https://doi.org/10.1002/adfm.202101724
WILEY-VCH

Carbon Nitride-Based Photoanode with Enhanced Photostability and Water Oxidation Kinetics

Neeta Karjule, Chanderpratap Singh, Jesús Barrio, Jonathan Tzadikov, Itamar Liberman, Michael Volokh, Emilio Palomares, Idan Hod and Menny Shalom**

Dr. Neeta Karjule, Dr. Chanderpratap Singh, Dr. Jesús Barrio, Jonathan Tzadikov, Itamar Liberman, Dr. Michael Volokh, Prof. Idan Hod and Prof. Menny Shalom
Department of Chemistry and Ilse Katz Institute for Nanoscale Science and Technology, Ben-Gurion University of the Negev, Beer-Sheva 8410501, Israel
E-mail: hodi@bgu.ac.il, mennysh@bgu.ac.il

Prof. Emilio Palomares
Institute of Chemical Research of Catalonia, The Barcelona Institute of Science and Technology (ICIQ-BIST), E-43007 Tarragona, Spain; Catalan Institution for Research and Advanced Studies, E-08010 Barcelona, Spain.

Keywords: Carbon nitride, photoelectrochemical cell, water splitting, metal-organic framework, cocatalyst

Carbon nitrides (CN) have emerged as promising photoanode materials for water-splitting photoelectrochemical cells (PECs). However, their poor charge separation and transfer properties, together with slow water-oxidation kinetics, have resulted in low PEC activity and instability, which strongly impede their further development. In this work, we address these limitations by optimizing the charge separation and transfer process. To this end, we deposit a nickel-iron based Metal-Organic Framework (MOF), Ni/Fe-MIL-53, that acts as an oxygen evolution pre-catalyst within the CN layer and incorporate reduced graphene oxide as an electron acceptor. Upon electrochemical activation, a uniform distribution of highly active oxygen evolution reaction (OER) catalysts is obtained on the porous CN surface. Detailed mechanistic studies reveal excellent hole extraction properties with high OER catalytic activity (83% faradaic efficiency) and long-term stability, up to 35 h. Our results indicate that the decrease in performance is mainly due to the slow leaching of the catalyst from the CN layer.

The CN photoanode exhibits a reproducible photocurrent density of 472 ± 20 μA cm^{-2} at 1.23 V *vs*. reversible hydrogen electrode (RHE) in 0.1 M KOH, an exceptionally low onset potential of ~ 0.034 V *vs*. RHE, and high external quantum yield.

1. Introduction

Converting solar energy into hydrogen *via* water-splitting photoelectrochemical cells (PEC) is a promising route for a sustainable energy supply.[1] In recent years, polymeric carbon nitride (CN) has emerged as an alternative to other widely researched photoanode materials in PEC, owing to its stability, low cost, and suitable energy bands position.[2] However, despite the progress in the development of CN photoanodes,[3] their PEC performances are still hindered by poor charge separation and transfer efficiency, as well as slow water oxidation kinetics, which results in fast charge-carrier recombination rates.[4] Moreover, a major limitation of CN photoanodes is their partial self-oxidation during PEC operation, which until now has resulted in low rates of oxygen production, even when relatively high photocurrents were obtained, i.e., low faradaic efficiency (FE). The resulting instability of the CN layer is another significant impediment to their long-term use.[5] Therefore, if substantial progress is to be made in the field of CN-based water-splitting PEC, these challenges must be addressed. The main reason for the self-oxidation of CN photoanodes lies in their sluggish catalytic OER reaction kinetics (OER = oxygen evolution reaction), allowing the accumulation of long-lived photogenerated holes, which in turn oxidize the CN layer.[6] To overcome the OER kinetic barrier, significant research efforts are ongoing to develop water oxidation catalysts to be used as electrolyzers or cocatalysts in photo(electro)chemical reactions.[7] Yet, to date, the inclusion of OER cocatalysts (e.g., $CoO(OH)_x$, IrO_x, Co-Pi, RuO_x, NiCo-LDH, and $NiFeO_x$) within CN-photoanode did not lead to significantly higher production of oxygen.[8]

Various Metal-Organic Frameworks (MOFs) have been used as precursors to obtain highly efficient OER catalysts, to make the most of their high content of active OER metal centers such as nickel, iron, and cobalt,[9] and also benefit from the high specific surface area, abundant

active sites, and significant porosity.[10] MOFs have emerged as particularly promising pre-catalysts for water oxidation; under catalytic operation, they are often converted into highly active oxide-hydroxide species,[11] which drive the reaction at high current densities and with low overpotentials, and are endowed with good long-term stability.[12] Recent studies have revealed that such binary Ni/Fe-based catalysts set the benchmark for OER catalysts thanks to the parent MOF properties and the synergistic effect of the two metals.[11b,13]

Herein, we report on the successful incorporation of an OER catalyst in a CN photoanode, with an associated improvement in its performance: the resulting photoanode shows high faradaic efficiency (up to 83%) for OER and hydrogen evolution reaction (HER), good long-term stability, and high external quantum yield, owing to excellent hole extraction efficiency and electron diffusion within the CN layer. The latter property was obtained by incorporating reduced graphene oxide within the layer.[14] The hole extraction efficiency was achieved by introducing a highly active Ni/Fe bimetallic MOF (Ni/Fe-MIL-53) as an OER pre-catalyst on the CN layer. This MOF precursor was prepared from a simple solvothermal reaction and, upon electrochemical activation, was converted into a highly active Ni/Fe cocatalyst ($NiFeO_xH_y$) with a uniform distribution along the CN layer. Detailed spectroscopic and (photo)electrochemical studies reveal excellent hole extraction efficiencies of up to 80%, high catalytic activity and selectivity, and good photostability of the photoanode. The CN photoanode exhibits a remarkable and reproducible photocurrent density of 472 ± 20 μA cm^{-2} at 1.23 V *vs.* reversible hydrogen electrode (RHE) in 0.1 M KOH and an extremely low onset potential of ~ 0.034 V *vs.* RHE.

2. Results and discussion

2.1. CN film preparation and characterization

Carbon nitride photoanodes which contain reduced graphene oxide (rGO) were prepared from melamine and graphene oxide using a two-step method involving doctor-blade and thermal

treatment,[3a] as shown in **Scheme 1**. Figures S1–S4 show detailed electrode preparation and characterization methods. Afterward, these CN-MR electrodes (MR stands for melamine-rGO as the precursor) were calcinated under inert atmosphere at elevated temperatures to condense melamine into CN and to reduce graphene oxide into rGO. CN modified with rGO structure provides better electron mobility, porous structure, and more electrochemically active surface sites.[14] Scanning electron microscopy (SEM) images of the CN-MR layer (~100 µm thick) show a porous structure, good coverage over the substrate, and intimate contact with the FTO substrate (Figure S5 and S6). Energy-dispersive X−ray spectroscopy (EDS) mapping confirms that carbon and nitrogen are uniformly distributed throughout the CN film (Figure S7). Figures S8–S12 contain additional characterization of the CN films and corresponding analysis.

2.2. MOF deposition onto the CN film and characterization

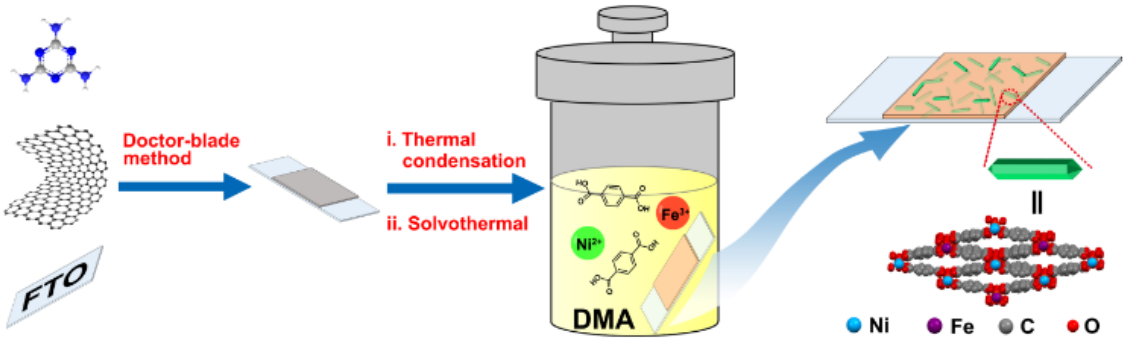

Scheme 1. Schematic preparation of CN-MR electrode followed by in situ synthesis of MOF (Ni/Fe-MIL-53) within the CN-MR film using a solvothermal reaction (the Ni/Fe-MIL-53 structure is depicted on the right side).

The OER pre-catalyst Ni/Fe-MIL-53 is a known mixed-metal MOF due to its excellent water oxidation properties.[9a] It was deposited onto the CN-MR films by placing a CN electrode in a solution containing the MOF precursors and proceeding to a solvothermal reaction in situ (**Scheme 1**). The precursors used in this reaction were $Ni(NO_3)_2 \cdot 6H_2O$, $FeCl_3$, and 1,4-benzene dicarboxylic acid (BDC) at a 2.4:1:1 molar ratio, and the solution was heated at 150 °C for 3

h.[11d] This selected Ni/Fe (2.4:1) molar ratio is optimal to afford bimetallic MOF with excellent OER performance.[9a,12d]

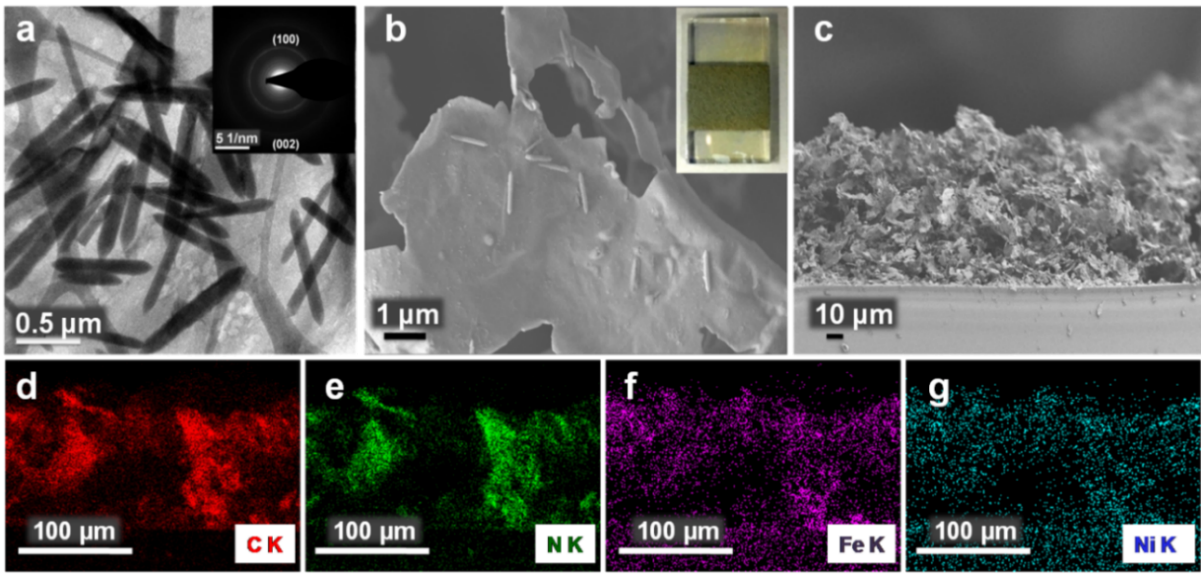

Figure 1. Electron microscopy characterization of a CN-MR/MOF photoelectrode. a) TEM image of CN-MR/MOF (inset: corresponding SAED pattern). SEM images of CN-MR/MOF: b) top view (inset: digital image of the CN-MR/MOF electrode) and c) cross-section. SEM EDS mapping of CN-MR/MOF showing the elemental distribution of d) carbon, e) nitrogen, f) iron, and g) nickel.

Transmission electron microscopy (TEM) images of the CN-MR/MOF reveal the presence of uniform rod-like MOFs nanocrystals with an average length of 0.83 ± 0.14 µm and an average diameter of 0.11 ± 0.02 µm (**Figure 1**a and Figure S13).[9a] Selected-area electron diffraction (SAED) discloses (002) and (100) diffraction rings, illustrating the crystalline structure of the MOF-modified CN films (**Figure 1**a inset). High-angle annular dark-field scanning TEM (HAADF-STEM) and energy-dispersive X-ray spectroscopy (EDS) mapping demonstrate a uniform elemental distribution of Fe, Ni, and O throughout the MOF (Figure S14). SEM images confirm that the MOF rods are distributed within the porous CN films (**Figure 1**b,c and Figure S15). The associated EDS mappings (cross-section) also show a

uniform distribution of C, N, O, Fe, and Ni in the film (**Figure 1**d–g, Figure S15, and Figure S16). X-ray diffraction (XRD) and X-ray photoelectron spectroscopy (XPS) measurements (Figure S17 and S18) confirm the successful formation of the bimetallic Ni/Fe-MIL-53 MOF within the CN-MR layer (see discussion in the Supplementary Information). Elemental analysis further supports the presence of Fe, Ni, and O, along with C and N elements derived from the CN framework (Table S1).

In Ni/Fe-based OER catalysts, Ni usually acts as the active center for the oxygen evolution reaction; the incorporation of Fe allows the tuning of the active site's electronic properties by inducing an anodic shift of the Ni^{3+}/Ni^{2+} peak potential.[9a,15] Cyclic voltammetry (CV) of the CN-MR/MOF samples was carried out in 0.1 M KOH (pH = 13.1) at a scan rate of 100 mV s^{-1} to convert the MOF into a highly active OER catalyst. Upon cycling, a reversible $Ni^{3+/2+}$ redox peak in the potential range of 1.3–1.5 V *vs.* RHE (**Figure 2**a and Figure S19a) gradually rises, which corresponds to the transformation of $Ni(OH)_2$ to NiOOH.[16] XRD patterns of the CN-MR/$NiFeO_xH_y$ films after electrochemical activation show the disappearance of the characteristic MOF diffraction reflections, indicating that the crystalline structure of the MOF changed to an amorphous one in the basic electrolyte (Figure S19b).[17] Raman analysis also confirmed the MOFs were electrochemically converted into metal–oxides-hydroxides ($NiFeO_xH_y$) (Figure S20).[11a,18] It should be noted that all the characterization and PEC measurements presented from this stage on were conducted after the activation of the CN-MR/MOF electrode by CV and the samples were denoted as CN-MR/$NiFeO_xH_y$.

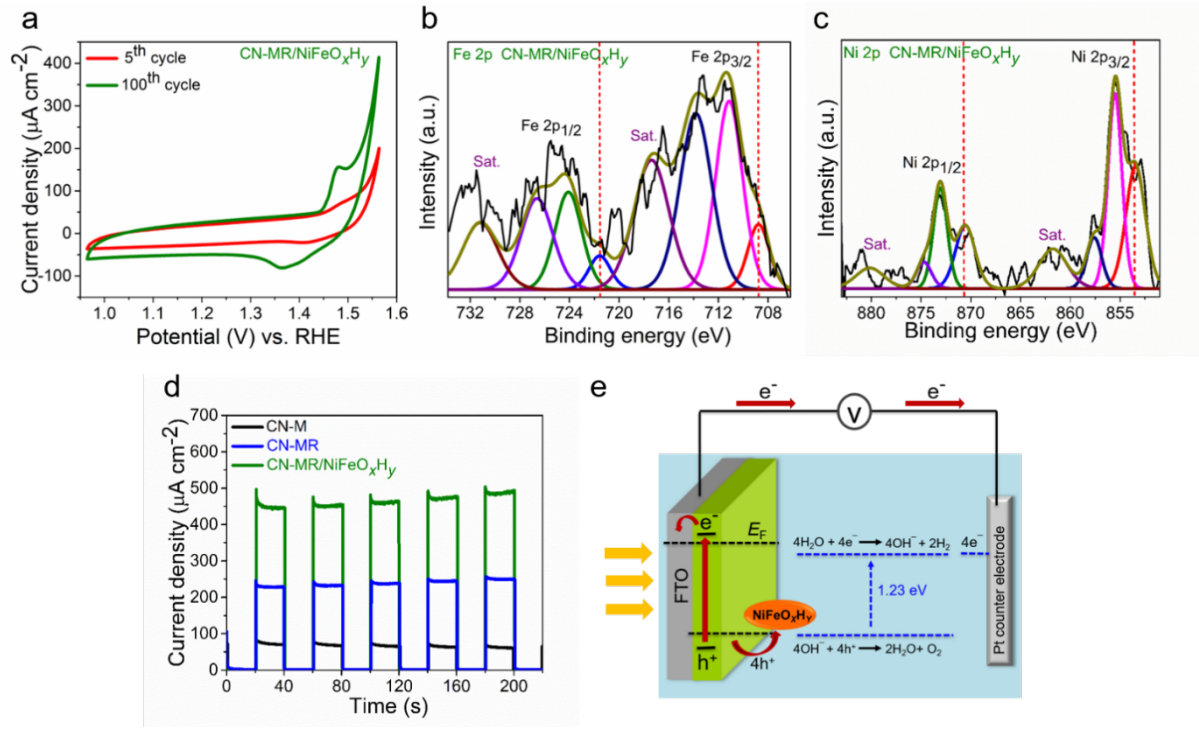

Figure 2. Electrochemical and photoelectrochemical characterization of photoanodes. a) Cyclic voltammograms of CN-MR/MOF in 0.1 M KOH. High-resolution XPS spectra of CN-MR/($NiFeO_xH_y$) electrodes after CV measurements for b) Fe 2p and c) Ni 2p. d) Chronoamperometry (photocurrent densities *vs*. time) of CN-M (black), CN-MR (blue), and CN-MR/($NiFeO_xH_y$) (green) electrodes in 0.1 M KOH (pH = 13.1). e) Suggested water splitting PEC (alkaline conditions) illustration scheme.

Detailed XPS spectra of the C 1s, N 1s, O 1s, Fe 2p, and Ni 2p were also recorded after the CV (**Figure 2**b,c and Figure S21): new distinct peaks located at lower binding energies are observed in the Fe 2p, Ni 2p, and O 1s XPS spectra.[19] The Fe $2p_{3/2}$ (or $2p_{1/2}$) and Ni $2p_{3/2}$ (or $2p_{1/2}$) electronic configurations are deconvoluted into three peaks and one satellite peak. The Fe $2p_{3/2}$ electronic configuration is deconvoluted into three peaks at 708.8, 711.1, and 713.9 eV corresponding to FeOOH, FeO, and $NiFeOH_x$, respectively, thus revealing that several types of iron species are present after the CV measurement (**Figure 2**b). In the nickel case, the deconvolution of the Ni $2p_{3/2}$ electronic configuration reveals three signals at binding energies of 853.4, 855.5, and 857.7 eV, which correspond to NiOOH, NiO, and $Ni(OH)_2$, respectively

(**Figure 2**c).[19b] The O 1s XPS spectrum indicates the presence of metal–oxide (M–O) bonds, metal hydroxide (M–OH) species, and adsorbed water or C–O, respectively (Figure S21). Notably, the O 1s spectrum shows the formation of metal–oxide and metal–hydroxide phases on the surface of the samples after CV. The XPS result indicates that a bimetallic catalyst is obtained and that the Ni and Fe species are in the +2 and +3 oxidation states.[20] Moreover, SEM EDS mapping after CV shows an even elemental distribution (C, N, O, Fe, and Ni) in the CN-MR/MOF films (Figure S22 and Table S2). Considering all the data mentioned above, we can conclude that the highly active Ni/Fe–(oxy)hydroxide ($NiFeO_xH_y$) OER cocatalysts are well-dispersed within the CN layer.[16]

2.3. Optical and electrochemical properties

The UV–vis absorption spectra show that the extent of light absorption and absorption edges of the CN-MR/$NiFeO_xH_y$ electrode are comparable to the CN-MR electrode (Figure S23a). The estimated optical band gap (E_g) of CN-MR is 2.69 eV, similar to the E_g of CN-MR/$NiFeO_xH_y$ (2.66 eV) (Figure S23b). The photoluminescence (PL) spectra show that the emission in the CN-MR and CN-MR/$NiFeO_xH_y$ films is quenched relative to that of the CN-M film (pristine melamine-based CN) (Figure S23c). A slight shift in the maximum wavelength from 468 nm to 451 nm also occurs. When the $NiFeO_xH_y$ is present, the PL intensity clearly decreases, indicating that the MOF-modified CN-MR film effectively suppresses the radiative recombination of photogenerated electron-hole pairs.[21] Typical FTIR spectra of the CN-MR film and Ni/Fe-MIL-53 are shown in Figure S24. The peak at 3158 cm^{-1}, a characteristic feature of CN, is made stronger and broader by the presence of metal–hydroxide. The flat-band potential of the electrodes, determined by electrochemical Mott-Schottky analysis (Figure S25), suggests an n-type behavior.[22] The conduction band (CB) of CN-MR and CN-MR/MOF is estimated to be −0.5 V and −0.65 V *vs*. RHE, respectively. According to their E_g, the valence band (VB) position of CN-MR and CN-MR/MOF is 2.19 V and 2.01 V *vs*. RHE, respectively.

2.4. Water-splitting PEC performance

The photoelectrochemical properties were measured under 1-sun illumination and 0.1 M aqueous KOH solution (pH = 13.1) as the electrolyte. All measurements were conducted on three separate batches of samples, to verify reproducibility and to calculate standard deviation. The CN-MR electrode displayed an increased photocurrent density (241 ± 10 μA cm^{-2} at 1.23 V *vs*. RHE) relative to the rGO-free carbon nitride (CN-M) electrode, as shown in **Figure 2**d. In the former, rGO acts as an electron-accepting layer and further increases the films' electric conductivity.[23] The CN-MR/$NiFeO_xH_y$ electrode showed a significant photoresponse enhancement in comparison with the CN-MR electrode and reached a stable photocurrent density of 472 ± 20 μA cm^{-2} at 1.23 V *vs.* RHE (**Figure 2**d). This improvement stems mainly from the ability of the OER cocatalyst to catalyze the hole transfer from the semiconductor to the electrolyte. Indeed, as the photocurrent consists of the separation and migration of photogenerated electron-hole pairs, a higher photocurrent indicates a more efficient electron diffusion and injection of holes into the electrolyte (**Figure 2**e).

Control experiments were carried out on the CN-MR electrodes to verify the necessity of using the MOF as the pre-catalyst: control electrodes were prepared via the same solvothermal reaction but (i) in the absence of MOF precursors (see chronoamperometry results in Figure S26) and (ii) in the presence of the MOF's Fe and Ni precursors but in the absence of BDC ligand (Figure S27). Neither electrode showed significant improvement in the photocurrent density over the CN-MR electrode (230 ± 20 μA cm^{-2} at 1.23 V *vs*. RHE, Figure S27). To demonstrate the MOF's uniqueness as a pre-catalyst, other known cocatalysts such as $CoO(OH)_x$, IrO_x, RuO_x, and $NiFeO_x$ have been investigated (Figure S28).[8a,24] However, no significant improvement in photocurrent density was observed. Furthermore, CN-MR photoanode modifications with nickel- and iron-based catalysts (NiOOH, FeOOH, and NiFe-LDH) did not significantly enhance the photocurrent and stability (Figure S29a).[25] These attempts of modifying CN-photoanodes with OER catalysts failed to provide the desired

improvement in OER kinetics, mainly due to a poor connection to the CN matrix, inhomogeneous distribution of the catalyst within the CN layer, or unsuccessful growth of the cocatalyst on the CN's surface. Additionally, a comparison was carried out between the electrochemical activity of (i) a MOF, which was converted into $NiFeO_xH_y$, and (ii) a directly-synthesized $NiFeO_xH_y$ (Figure S29b).[26] The photocurrent density slightly increases in the presence of the directly-synthesized $NiFeO_xH_y$ cocatalyst (300 ± 15 μA cm^{-2}). Unlike unmodified CN-MR or CN-MR modified with MOF converted into $NiFeO_xH_y$, the photocurrent was not stable.

Photocurrent measurements upon back- and front-side illumination (Figure S30) suggest that the layer's thickness is not optimal: lower currents were obtained for front illumination owing to the long distance that the photoexcited electrons must travel before reaching the FTO. During photocurrent measurements, an initial "spike current" is observed, which arises from photoelectron recombination with surface-trapped holes or photo-oxidation intermediates.[27]

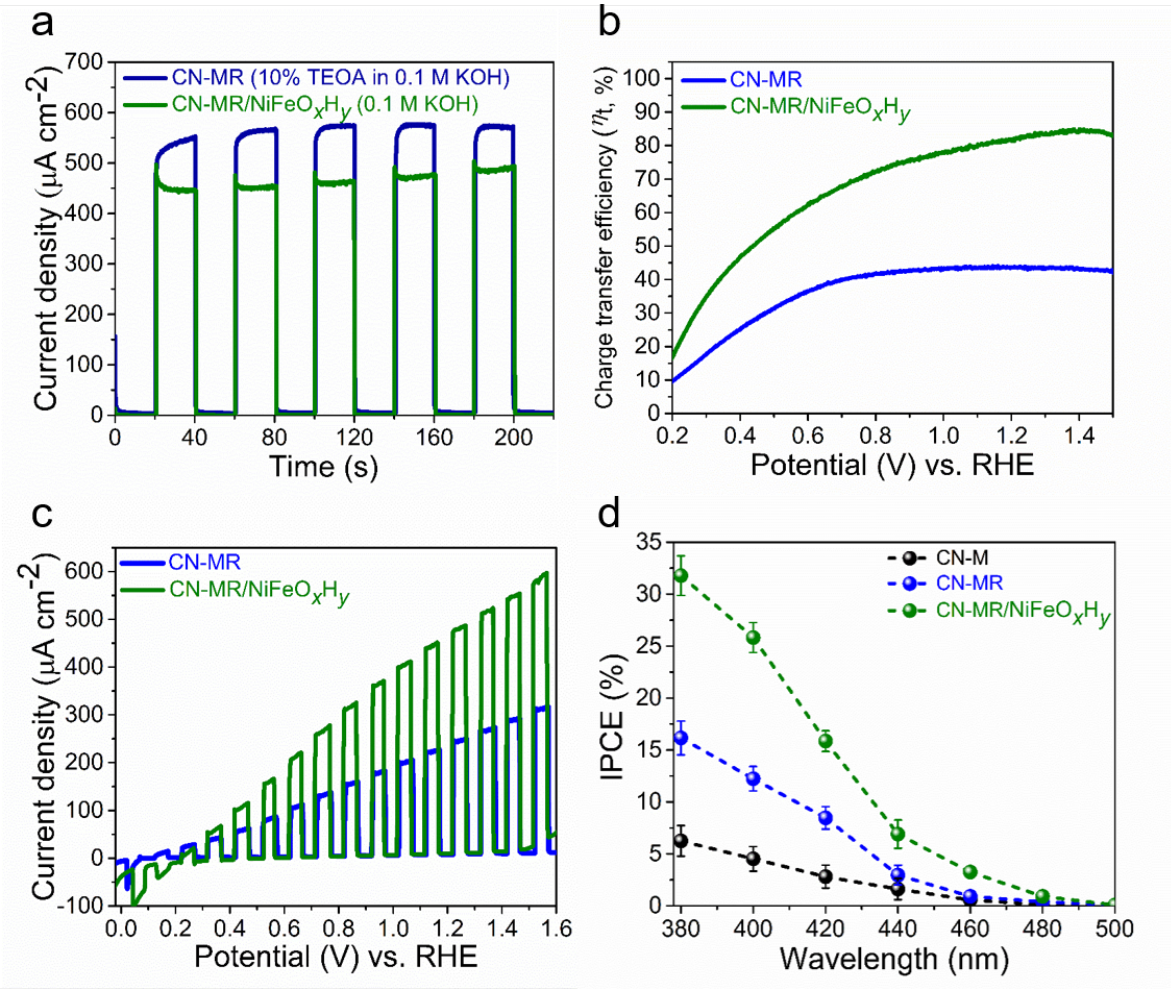

Figure 3. Photoelectrochemical characterization of photoanodes. a) Chronoamperometry of CN-MR (dark blue) in 0.1 M KOH in the presence of 10% TEOA (v/v) as a hole scavenger compared to CN-MR/NiFeO$_x$H$_y$ (green) in 0.1 M KOH only. b) Calculated charge transfer efficiency of the CN electrodes. c) LSV curves of CN-MR and CN-MR/NiFeO$_x$H$_y$ under on/off illumination. d) IPCE of CN-based electrodes at different wavelengths in 0.1 M KOH aqueous solution at 1.23 V *vs.* RHE (The error bars represent the standard deviations over three independent measurements).

The hole-extraction efficiency of each sample was obtained by comparing the photocurrent density of the electrode in the presence and absence of triethanolamine (TEOA) as a fast hole acceptor (10% TEOA (v/v) in 0.1 M KOH, see Figure S31). The CN-MR electrode exhibits a

two-fold photocurrent density enhancement (563 ± 17 μA cm^{-2} at 1.23 V *vs.* RHE) in the presence of TEOA, owing to the improved hole extraction. The CN-MR/$NiFeO_xH_y$ electrode, on the other hand, exhibits a photocurrent density of 598 ± 12 μA cm^{-2} at 1.23 V *vs.* RHE, i.e., an increase of only *ca.* 27%, in the presence of a hole scavenger. **Figure 3**a presents a comparison between the CN-MR photoanode in 10% TEOA (v/v) in 0.1 M KOH and CN-MR/$NiFeO_xH_y$ in 0.1 M KOH only. Interestingly, the photocurrent density of CN-MR/$NiFeO_xH_y$ without hole scavenger reaches about 84% of the value for CN-MR in the presence of a hole scavenger. This result clearly demonstrates an improved charge transfer associated with the incorporation of the $NiFeO_xH_y$ cocatalyst, which we attribute to the facile hole extraction by the cocatalyst and faster water oxidation kinetics.[18,28] For the CN-MR photoanode, the charge-transfer efficiency reaches 44% at 1.23 V *vs.* RHE. Remarkably, the charge-transfer efficiency of CN-MR/$NiFeO_xH_y$ is enhanced to more than 80% at 1.23 V *vs.* RHE after the $NiFeO_xH_y$ incorporation and remains higher than 50% in the 0.4–1.23 V *vs.* RHE region (**Figure 3**b). HER via PEC water-splitting in the presence of 10% (v/v) TEOA in 0.1 M KOH was quantified by gas chromatography (GC, Figure S32). CN-MR/$NiFeO_xH_y$ exhibited continuous H_2 generation over time (24.1 μmol cm^{-2} of H_2 produced after 3 h of illumination). The overall faradaic efficiency in the presence of a hole scavenger for CN-MR/$NiFeO_xH_y$ reached 97.3%, compared to only 57.2% for the pristine CN (CN-M). Linear sweep voltammograms (LSV) were recorded under on/off light illumination (**Figure 3**c). The CN-MR/$NiFeO_xH_y$ films demonstrated a significant photoresponse enhancement, with an extremely low onset potential (0.034 V), contrasting with the onset potential of CN-MR of about 0.12 V (Figure S33); this implies a better charge separation under illumination for the former. CN-MR/$NiFeO_xH_y$ shows a photocathodic response with a photocurrent density *ca.* 36 μA cm^{-2} at 0 V *vs.* RHE (Figure S34). Incident photon-to-current efficiency (IPCE) measurements from 380 to 500 nm at 1.23 V *vs.* RHE are presented in **Figure 3**d. The IPCE values for the CN-MR/$NiFeO_xH_y$ and CN/MR photoanodes at λ = 380 nm are 32 ± 2% and 16 ± 2%, respectively,

corresponding to a 5- and 2.6-fold enhancement over pristine carbon nitride photoanodes (CN-M, 6 ± 1%). Notably, the IPCE onset is comparable in the CN-MR and CN-MR/NiFeO$_x$H$_y$ photoanodes (ca. 480 nm), in line with the resemblance of their optical absorption edge.

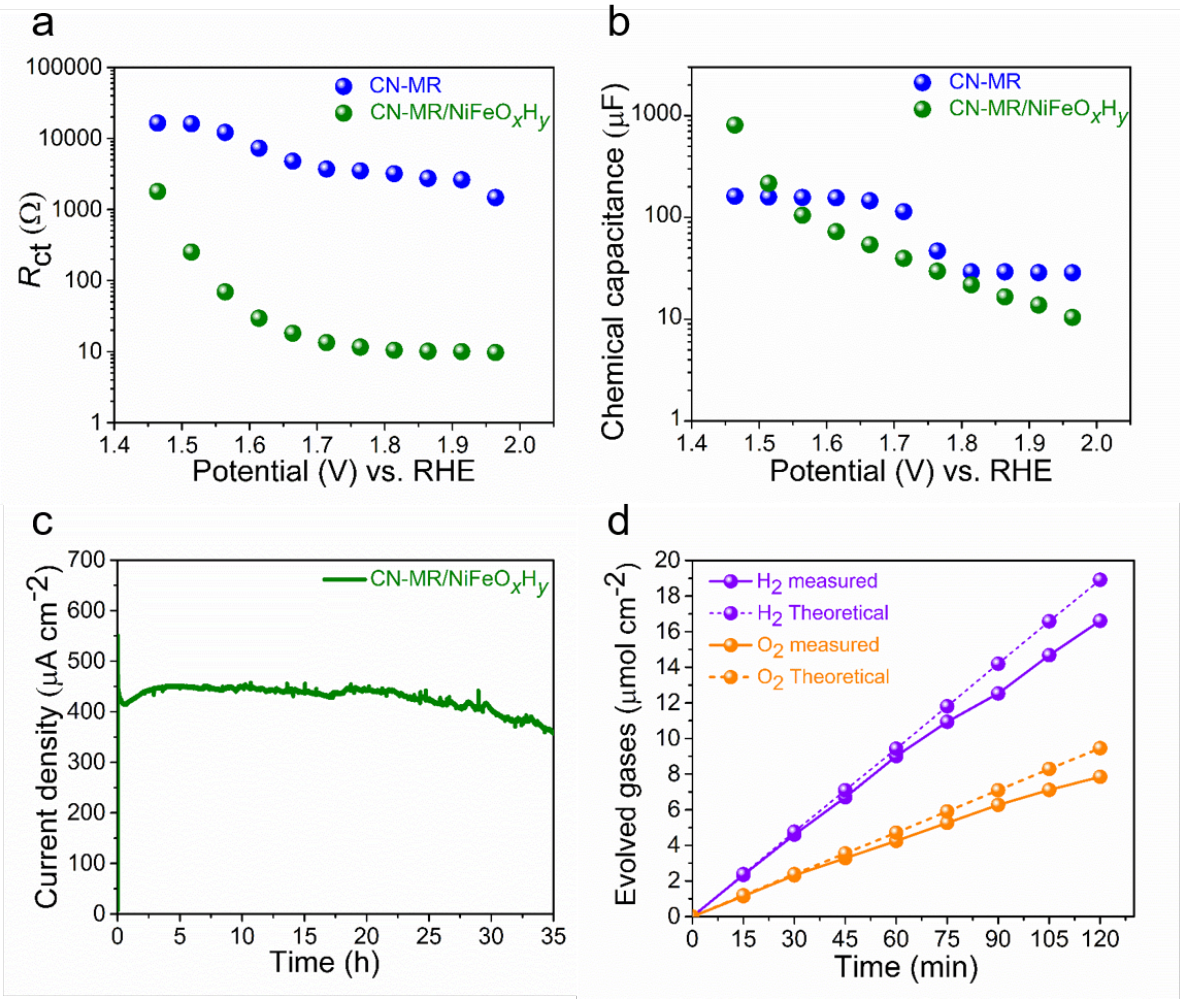

Figure 4. Electrochemical and photoelectrochemical characterization of photoanodes. a) Charge transfer resistance (R_{ct}) and b) Chemical capacitance of the CN-MR/NiFeO$_x$H$_y$ electrodes at different applied potentials. c) Chronoamperometry (current density *vs.* time) for CN-MR/NiFeO$_x$H$_y$ at 1.23 V *vs.* RHE under simulated 1-sun illumination for 35 h. d) Evolution of H_2 and O_2 gases measured by gas chromatography (dashed lines correspond to the expected amount of H_2 and O_2 calculated from the photocurrent measurements).

The CN-MR and CN-MR/NiFeO$_x$H$_y$ electrodes were analyzed by electrochemical impedance spectroscopy (EIS) at applied DC potentials of 1.47–1.97 V *vs.* RHE (**Figure 4**a,b

and Figure S35). Charge transfer resistance (R_{ct}) and chemical capacitance (C_{μ}) were extracted by fitting the semicircles of the Nyquist plots using the equivalent circuit shown in Figure S35d. R_{ct} values indicate the charge transfer resistance from the electrode to the electrolyte. It demonstrates that the cocatalyst enhances the hole transfer kinetics to the electrolyte: the presence of a cocatalyst significantly reduces the charge transfer resistance (R_{ct}) of the material (**Figure 4**a).[29] The C_{μ} (**Figure 4**b) of the two electrodes is similar, implying a catalytic effect rather than surface passivation or a change in the semiconductor's nature (e.g., density of states, energy band edges).[30] In congruence with the difference in R_{ct}, CN-MR/NiFeO$_x$H$_y$ exhibits drastically lower hole lifetimes (τ) than CN-MR throughout the entire applied potential range (up to 3 orders of magnitude lower, as shown in Figure S35c). The inclusion of rGO and NiFeO$_x$H$_y$ dramatically increases the electrochemical active surface area (ECSA), thus providing more solution-accessible catalytic sites (Figure S36). Fluorescence lifetime measurements of all the electrodes further corroborate the improvement in the charge separation under illumination. Fewer emission counts and shorter lifetimes are observed, which shows that the rGO and the cocatalyst suppress charges recombination (Figure S37).[31]

To investigate the influence of pH on the performance and stability of the photoanode, we recorded the PEC performance of the electrodes in acidic (0.5 M H_2SO_4, pH = 0.27) and neutral electrolytes (0.5 M Na_2SO_4, pH = 6.27) using chronoamperometry (1.23 V *vs.* RHE, Figure S38). The photocurrent density of CN-MR/NiFeO$_x$H$_y$ reaches 350 ± 16 μA cm^{-2} in acidic medium, despite the sluggish oxidation reaction at low pH. However, the instability of the cocatalyst under acidic conditions hinders its further use in PEC. In a neutral solution, a current density up to 400 ± 15 μA cm^{-2} is obtained.

Interestingly, when the MOF-precatalyst loading is increased three-fold, the recorded photocurrent density is less stable (Figure S39), owing to catalyst aggregation: this results in the formation of excess recombination centers, which shorten the electron–hole pairs'

lifetime.[32] SEM images clearly show the aggregation of MOFs within the CN films at these conditions (Figure S40).

A major challenge in the use of CN and other photoanode materials in water oxidation PEC is their poor long-term stability under operating conditions. As shown in **Figure 4**c, in the presence of the cocatalyst, the photocurrent density obtained with CN-MR/ $NiFeO_xH_y$ is stable for up to 22 h in 0.1 M KOH aqueous solution. In comparison, the CN-MR photoanode loses 34% of its initial photocurrent over a 9 h stability test (Figure S41a). Importantly, for the CN-MR layer, a large part of the photocurrent is attributed to self-oxidation of the CN and not to the oxidation of water. The faradaic efficiency for H_2 and O_2 production of the electrodes was measured under 1-sun AM 1.5G (100 mW cm^{-2}) irradiation at 1.23 V *vs.* RHE in two-compartment cell (Figure S42). For CN-MR/$NiFeO_xH_y$, the ratio of O_2 to H_2 is close to stoichiometric, and the faradaic efficiencies for HER and OER are about 87.8 ± 3% and 83.0 ± 5%, respectively (**Figure 4**d). In contrast, the OER faradaic efficiency of CN-MR is 15.6 ± 3% only (Figure S41b). These results confirm that, for CN-MR/$NiFeO_xH_y$, the measured photocurrent results mainly from the water oxidation reaction, as opposed to the $NiFeO_xH_y$-free CN-MR, where self-oxidation plays a prominent role. Additionally, the evolution of H_2 and O_2 was studied in a phosphate buffer solution (0.1 M; pH 7 at 1.23 V *vs*. RHE). CN-MR/$NiFeO_xH_y$ showed a current density up to 320 ± 28 μA cm^{-2} in phosphate buffer solution, with faradaic efficiencies for HER and OER at about 54.0% and 43.8%, respectively (Figure S43).

To assure that the detected oxygen arises from the CN-MR/$NiFeO_xH_y$ electrode, a scanning electrochemical microscopy (SECM) measurement was employed.[30,33] This experiment was performed with a substrate (CN-MR/$NiFeO_xH_y$) generation-tip (5 μm Pt-based ultramicroelectrode) collection mode, both in the dark and under illumination (l = 405 nm), for the direct detection of O_2 by the microelectrodes, positioned in close proximity to the CN-MR/$NiFeO_xH_y$ (Figure S44 and S45; further details are provided in the methods section). We conclude that the oxidative substrate photocurrent followed by a reductive tip current provides

a direct confirmation of photoelectrocatalytic O_2 generation using a CN-MR/MOF photoanode (Figure S44).

Detailed characterization was performed on the CN-MR/$NiFeO_xH_y$ and CN-MR electrodes after a long-term stability test (35 h and 9 h, respectively) to assess their structural properties after long-term measurements. XPS measurements reveal a small decrease in the C-to-N atomic ratio (from 1.41 to 1.24), suggesting a minor degradation of the CN framework. The relatively high amount of oxygen indicates the presence of metal hydroxides and physically adsorbed H_2O (Figure S46 and Table S3). Interestingly, the morphology of the CN structure is preserved in CN-MR/$NiFeO_xH_y$ (Figure S47). The estimated amount of Ni decreases from 3.71 at.% to 1.25 at.% and the Fe 2p signal vanishes. Inductively coupled plasma optical emission spectrometry analysis (ICP-OES) reveals that some dissolution of Ni and Fe into the electrolyte (0.1 M KOH) occurs: Ni and Fe contents of about 1.65 and 0.3 ppm, respectively, were detected. XPS measurements of CN-MR after the long-term stability test indicate no significant structural changes in the CN films (Figure S48). The post-test characterization shows that the main reason behind the slow deactivation lies in the Ni and Fe leaching during the long stability measurements of CN-MR/$NiFeO_xH_y$. To confirm this, the amount of photogenerated H_2 and O_2 in the reactor headspace was analyzed by GC after the stability test and showed no O_2 production; only H_2 was produced. Nevertheless, the CN-MR/ $NiFeO_xH_y$ maintains more than 87% of its initial activity even after 35 h. Moreover, monometallic MOF (Ni-MOF and Fe-MOF) were deposited separately on CN-MR electrodes. The stability of these photoanodes was tested after electrochemical activation. No significant improvement in stability nor photocurrent density was observed (Figure S49). Therefore, we believe that a synergy between multiple metal atoms (Ni, Fe) is crucial for high OER catalytic activity.[34] Overall, the results show that the $NiFeO_xH_y$-modified CN-MR photoanode exhibits higher photoelectrochemical activity than that reported so far for other CN photoanodes (Table S4).

3. Conclusion

To overcome the main bottleneck (i.e., the slow water oxidation rate) in CN photoanodes for water splitting, we used a MOF as a precursor (pre-catalyst) for the in situ synthesis of an OER cocatalyst ($NiFeO_xH_y$). Consequently, we achieved a substantial improvement in stability and faradaic efficiency (efficiency > 80%) for oxygen and hydrogen production in alkaline solution. The addition of the highly active OER cocatalyst within the porous CN layer ensures fast and effective hole removal and, and along with the inclusion of reduced graphene oxide as an electron acceptor, optimizes the charge separation and transfer. Structural characterizations reveal a uniform distribution of Ni-Fe catalysts within the material with a good connection to the CN matrix. The resulting fast charge separation and excellent hole extraction efficiency (up to 80%) are responsible for the reported progress in the long-term stability and high catalytic activity for O_2 production. The best CN photoanode exhibits a high photocurrent density of 472 ± 20 μA cm^{-2} at 1.23 V *vs.* RHE in 0.1 M KOH, low onset-potential at ~ 0.034 V *vs.* RHE, positioning CNs as promising metal-free photoanode materials in PEC. Long-term stability tests reveal a slow degradation of the performance of the electrode. We have established that the primary mechanism for this degradation is the slow leaching of the OER catalyst: future research efforts will be directed to further reducing this process.

4. Experimental section

Materials: All chemicals were purchased from commercial sources and used without further purification. Ethylene glycol (EMSURE® Reag. Ph. Eur, Reag. USP) was purchased from Merck. Melamine (99%), nickel (II) nitrate hexahydrate ($Ni(NO_3)_2 \cdot 6H_2O$, ≥97%), iron (III) chloride ($FeCl_3$, 97%), 1,4-benzendicarboxylic acid (BDC, 98%), and potassium chloride (ReagentPlus®, ≥99.0%) were purchased from Sigma-Aldrich. Ethanol and dimethylformamide (DMF) were purchased from Bio-Lab Ltd., Israel. Triethanolamine (TEOA, 99%) was purchased from Glentham Life Sciences, UK. *N*,*N*-dimethylacetamide

(DMA, 99.5%), sodium sulphate anhydrous (Na_2SO_4, 99%), and potassium hydroxide pellets (KOH, 85%) were purchased from Loba Chemie, India. Potassium ferricyanide (III) ($K_3[Fe(CN)_6]$, 99%) was obtained from Fluorochem, UK. Nitric acid (HNO_3, 67–69%, for trace metal analysis) was obtained from Fisher Chemical. Fluorine-doped tin oxide (FTO) coated glass (12–14 Ω sq^{-1}) was purchased from Xop Glass Company, Spain. Nafion™ perfluorinated membrane (Nafion 117) was purchased from Sigma-Aldrich. Pt capillary-based ultramicroelectrodes (UME) (a = 5 μm, RG = 10) were purchased from Bio-Logic Science Instruments. De-ionized water (DI) was purified using a Millipore Direct-Q® 3 water purification system (18.2 MΩ cm resistivity). Graphene oxide (GO, 0.4 wt.%, >95%) aqueous suspension was purchased from University Wafer Inc., USA (C89/GOSD18004/D).

Electron microscopy: Scanning electron microscopy (SEM) images of the CN electrodes were obtained using a JEOL JSM-7400F high-resolution SEM, equipped with a FEG source, operated at an accelerating voltage, U_0 = 3.5 or 4.0 kV (after sputtering with Pt, ~7 nm using Quorum Q150T ES system). Energy-dispersive X-ray spectroscopy (EDS) elemental mappings were obtained using a FEI Verios 460L high-resolution SEM equipped with a FEG source and operated at U_0 = 12 kV (CN-MR) and U_0 = 20 kV (CN-MR/MOF). Transmission electron microscopy (TEM) images were obtained using a Tecnai (FEI) T12 G^2 TWIN microscope at U_0 = 120 kV. EDS analysis on an analytical TEM was performed using a JEOL JEM-2100F TEM (U_0 = 200 kV) equipped with a JED-2300T energy dispersive X-ray spectrometer. Scanning TEM (STEM) images were taken using a GATAN 806 HAADF STEM detector. The probe size during the analysis was set to 1 nm. JEOL Analytical Station software (v. 3.8.0.21) was used for EDS data analysis.

Optical characterization: UV–vis absorption spectra were measured on a Cary 100 spectrophotometer. Fluorescence measurements were carried out on a FluoroMax® 4 spectrofluorometer from Horiba Scientific. The Time-correlated Single Photon Counting (TCSPC) measurements were performed using an Edinburgh Instruments LifeSpec II

spectrometer. The excitation wavelength was 405 nm and the emission wavelength was 475 nm. The acquisition was carried out fixing the maximum number of emission counts to $5´10^3$ and the measurements were carried out under ambient conditions (room temperature, in air, under atmospheric pressure). All CN samples were measured 3 times to ensure reproducibility with negligible differences. Fourier-transform infrared spectroscopy (FTIR) was performed on a Thermo Scientific Nicolet iS5 FTIR spectrometer (equipped with a Si ATR).

Structural and compositional characterization: X-ray diffraction patterns (XRD) were obtained using a PANalytical's Empyrean diffractometer equipped with a position-sensitive detector X'Celerator. Data was collected with a scanning time of ~7 min for 2θ ranging from 5° to 60° using Cu Kα radiation (λ = 1.54178 Å, 40 kV, 30 mA). The Raman spectrum was obtained by using a LabRam HR high-resolution analytical Raman instrument using an excitation wavelength of 532 nm. X-ray photoelectron spectroscopy (XPS) data were obtained from an X-ray photoelectron spectrometer ESCALAB 250 ultrahigh vacuum (1×10^{-9} bar) device with an Al Kα X-ray source and a monochromator. The X-ray beam size was 500 μm, survey spectra were recorded with a pass energy (PE) of 150 eV and high energy resolution spectra were recorded with a PE of 20 eV. To correct for charging effects, all spectra were calibrated relative to a carbon C 1s peak, positioned at 284.8 eV. The depth profile of the sample was obtained by combining a sequence of Ar ion gun etch cycles (250 s) interleaved with XPS measurements from the current surface. The sputtering rate was approximately 0.07 nm s^{-1}. The XPS results were processed using the Thermo Scientific™ Avantage software**.** Elemental analysis data for carbon, nitrogen, and hydrogen (CNH) was collected using a Thermo Scientific Flash Smart elemental analyzer OEA 2000. After (the electrochemical) stability test, 100 μL of electrolyte was used to measure the Ni and Fe content by inductively coupled plasma optical emission spectrometry (ICP-OES). Samples were prepared by dissolution in concentrated nitric acid in a PTFE-lined autoclave at 180 °C for 8 h. Then, the prepared samples were analyzed using a Spectro ARCOS ICP-OES, FHX22 multi-view plasma instrument (Radial configuration).

Nitrogen-sorption measurements and Brunauer-Emmet-Teller (BET) specific surface area calculations were performed on a Quantachrome NOVAtouch NT LX^3 system. The thickness of CN films was measured by 3D laser confocal scanning microscopy (LEXT OLS5000).

Melamine and MG film preparation: For the preparation of the melamine-graphene oxide (MG) supramolecular paste, melamine powder (2.0 g) was blended thoroughly in ethylene glycol (1.4 mL) with graphene oxide aqueous suspension (1.0 mL, 0.8 wt.% GO suspension was prepared by concentrating commercial GO of 0.4 wt.%). The obtained paste was doctor-bladed (with 2 scotch tape layers (*L*) in order to control the thickness) onto FTO-coated glass to achieve a homogeneous coating, subsequently dried at 90 °C on a hot plate, and finally transferred into a closed (not sealed) 16 mm-diameter glass test tube. Note that all the FTO substrates were cleaned by successive sonication in an aqueous detergent solution (1% w/v Alconox), acetone, and ethanol, and were finally dried before usage. Melamine films were prepared by grinding (mortar and pestle) melamine powder (2.0 g) in ethylene glycol (1.2 mL) until obtaining a viscous paste.

Synthesis of CN electrode: For the calcination process, two electrodes were kept in a 16 mm-diameter glass test tube. The test tube was purged very carefully with nitrogen gas for 5 min and then covered with aluminum foil. Then, the samples were heated up to 550 °C at a ramp rate of 5 °C min^{-1} and kept at 550 °C for 4 h under a flow of N_2 to get CN-M and CN-MR electrodes.

Synthesis of bi-metallic MOF (Ni/Fe-MIL-53):[9a,11d] The in situ synthesis of Ni/Fe-MIL-53 in the CN electrodes was performed *via* a solvothermal method (the solvothermal procedure was adapted from reference 11d). First, the organic linker BDC (66.4 mg) was dissolved in DMA (28 mL) in one flask, whereas the metal salts $FeCl_3$ (64.9 mg) and $Ni(NO_3)_2{\cdot}6H_2O$ (279.6 mg) were dissolved in another flask containing 20 mL DMA using ultra-sonication. Then, both solutions were mixed under (magnetic PTFE coated stir-bar) stirring. An equal volume of the final mixture was transferred into four separate 20 mL PTFE vessels, and the as-prepared CN-

MR electrode was kept at the bottom of said vessels. Finally, the vessels were packed inside stainless-steel autoclaves and kept under a constant temperature of 150 °C for 3 h. After 3 h, the CN electrodes were removed from the vessels and washed twice, in a sequential manner, with the following solvents: DMF, water, and ethanol. They were then dried at 80 °C in a vacuum oven overnight.

The preparation process of monometallic MOF (Ni-MOF or Fe-MOF) was the same as that of bimetallic MOF except without the other metal salts.

Photoelectrochemical measurements: All electrochemical measurements were performed using a three-electrode system on an Autolab potentiostat (Metrohm, PGSTAT302N). A Pt-foil (1 cm^2) and Ag/AgCl (saturated KCl) were used as the counter and reference electrodes, respectively. The electrolyte was either 0.1 M KOH aqueous solution (pH = 13.1) or 0.1 M KOH solution containing 10% (v/v) TEOA. All the potentials were converted to reversible hydrogen electrode (RHE) values using equation 1.

Equation 1. $$V_{RHE} = V_{Ag/AgCl} + 0.059 \times pH + 0.197 \text{ (V)}$$

Photocurrents were measured at 1.23 V versus (*vs.*) RHE under the illumination of a solar simulator (Newport 300 W Xe arc lamp, equipped with an AM 1.5 G and water filters) at a power density of 100 mW cm^{-2}, which was calibrated using a thermopile power meter (Model 919-P, Newport), i.e., 1-sun conditions. For reporting photocurrent, a standard deviation (*s*) from three independent experiments (separate electrode preparation batches and different PEC measurements with new electrolytes) was calculated, and the values are presented as average photocurrent ± *s*. Incident photon-to-current conversion efficiency (IPCE) values were calculated using equation 2.

Equation 2. $$\text{IPCE (\%)} = \frac{J\,(\text{A cm}^{-2}) \times 1240}{\lambda\,(\text{nm}) \times I\,(\text{W cm}^{-2})} \times 100\%$$

where λ is the wavelength of the incident monochromic light, I is the incident illuminating power, J is the measured photocurrent density, and 1240 is the conversion factor. The

monochromic incident light with wavelengths of 380 nm, 400 nm, 420 nm, 440 nm, 460 nm, 480 nm, and 500 nm was generated by coupling the solar simulator with the corresponding band-pass filter (all band-pass filters were purchased from Thorlabs, Germany: FB380-10, FB400-10, FB420-10, FB440-10, FB460-10, FB480-10, and FB500-10, respectively). Charge transfer efficiency (h_t, %) was calculated by dividing the photocurrent obtained in the absence of the hole scavenger by the photocurrent obtained in its presence. Nyquist plots of the samples were measured in the frequency range from 100 kHz to 10 mHz at an applied voltage of 1.23 V *vs.* RHE. The time constant (τ) was calculated using equation 3.

Equation 3. $\tau = R_{ct} \times C_{\mu}$

Hydrogen and oxygen evolution measurements: The amount of photogenerated H_2 and O_2 in the reactor headspace was analyzed using a gas chromatograph (Agilent 7820 GC system) equipped with a thermal conductivity detector (TCD). Samples of gases were intermittently withdrawn every 15 min with an A-2 Luer lock gas syringe series purchased from VICI® precision sampling (Pressure-lok® precision analytical syringe). Two-compartment cells were thoroughly sealed with rubber septa and parafilm to prevent any gas leakage. Before all measurements, the electrolyte was purged with Ar for 30 min. The electrode was continuously held at 1.23 V (*vs.* RHE) under illumination.

Faradaic efficiency was calculated using equation 4.

Equation 4. $\text{Faradaic efficiency (\%)} = \frac{\text{experimental µmol of gas}}{\text{theoretical µmol of gas}} \times 100\%$

The theoretical amount of gas was calculated from Faraday's law, equation 5.

Equation 5. $n = \frac{I \times t}{z \times F} \times 100\%$

where n is the gas amount (measured in mol), I is the current (Ampere), t is the time (seconds), z is the number of transferred electrons (for H_2, $z = 2$; for O_2, $z = 4$), and F is the Faraday constant (96,485 C mol^{-1}).

Scanning electrochemical microscopy (SECM): Scanning electrochemical microscopy (SECM) measurements were performed on the CN-MR/NiFeO$_x$H$_y$ electrodes, utilizing a BioLogic SECM-150 workstation. The measurements were performed in a 0.1 M KOH solution (pH = 13.1), where the CN-MR/NiFeO$_x$H$_y$ film functions as the substrate, a Pt ultramicroelectrode (UME) with a radius (*a*), of 5 μm (RG = 10) is utilized as the SECM tip, while Ag/AgCl (saturated KCl) and Pt wire served as the reference and counter electrodes, respectively. In the SECM substrate generation tip-collection measurements, the potential on the tip was kept constant at 0.164 V *vs.* RHE, while the potential on the substrate was swept from 0.31 V to 1.7 V (*vs.* RHE) with a scan rate of 10 mV s^{-1}. The measurements were performed under illumination using a 405 nm light-emitting diode (LED) M405L4 from Thorlabs; light intensity: 13.94 mW cm^{-2}, LED driving current: 600 mA. Before the measurement, the gap spacing (*Z*) between the tip and a substrate was determined by monitoring the tip position, using an aqueous solution containing 5.0 mM ferricyanide ($K_3[Fe(CN)_6]$) and 0.1 M KCl, while keeping the tip at a constant potential of –0.3 V *vs.* Ag/AgCl. The obtained approach curves were fitted using MIRA SECM simulation software to extract the substrate-to-tip distance accurately. First, the Pt tip was placed in close proximity to the photoanode's surface (8 μm, see approach curves in Figure S43). Then, the illumination was turned on, and the substrate potential was scanned anodically to generate O_2. Simultaneously, direct O_2 detection was performed by fixing the tip potential at 0.164 V *vs.* RHE to successfully reduce substrate-evolved O_2 at a mass-transport limited rate.

Supporting Information

Supporting Information is available from the Wiley Online Library or from the author.

Acknowledgements

This project has received funding from the European Research Council (ERC) under the European Union's Horizon 2020 research and innovation programme (grant agreement No. [849068]). This work was also partially supported by the Israel Science Foundation (ISF), grant No. 1161/17, and ISF-NSFC grant No. 2969/19. The authors thank Liel Abisdris and Adi Azoulay for help with material characterization, Dr. Mariela Pavan for Raman measurements, and Dr. Jiawei Xia for help with picture art. We thank Dr. Chabanne for fruitful discussion.

Conflicts of interest

There are no conflicts to declare.

Received: ((will be filled in by the editorial staff))
Revised: ((will be filled in by the editorial staff))
Published online: ((will be filled in by the editorial staff))

References

[1] a) K. Sivula, R. van de Krol, *Nat. Rev. Mater.* **2016**, *1*, 15010; b) R. Abe, *J. Photochem. Photobiol. C* **2010**, *11*, 179.

[2] a) Y. Zhang, M. Antonietti, *Chem. Asian J.* **2010**, *5*, 1307; b) J. Barrio, M. Volokh, M. Shalom, *J. Mater. Chem. A* **2020**, *8*, 11075; c) Y. Wang, X. Wang, M. Antonietti, *Angew. Chem. Int. Ed.* **2012**, *51*, 68; d) C. Huang, Y. Wen, J. Ma, D. Dong, Y. Shen, S. Liu, H. Ma. Y. Zhang, *Nat. Commun*. **2021**, *12*, 320.

[3] a) N. Karjule, J. Barrio, L. Xing, M. Volokh, M. Shalom, *Nano Lett.* **2020**, *20*, 4618; b) G. Peng, J. Albero, H. Garcia, M. Shalom, *Angew. Chem. Int. Ed.* **2018**, *57*, 15807; c) T. Zhao, Q. Zhou, Y. Lv, D. Han, K. Wu, L. Zhao, Y. Shen, S. Liu, Y. Zhang, *Angew. Chem. Int. Ed*. **2020**, *59*, 1139.

[4] M. Volokh, G. Peng, J. Barrio, M. Shalom, *Angew.Chem. Int. Ed.* **2019**, *58*, 6138.

[5] a) W. Xiong, F. Huang, R. Q. Zhang, *Sustain. Energy Fuels* **2020**, *4*, 485; b) N. Karjule, R. Phatake, M. Volokh, I. Hod, M. Shalom, *Small Methods* **2019**, *3*, 1900401; c) W. Zhang, J. Albero, L. Xi, K. M. Lange, H. Garcia, X. Wang, M. Shalom, *ACS Appl. Mater. Interfaces* **2017**, *9*, 32667.

[6] a) Y. Kuang, T. Yamada, K. Domen, *Joule* **2017**, *1*, 290; b) M. G. Walter, E. L. Warren, J. R. McKone, S. W. Boettcher, Q. Mi, E. A. Santori, N. S. Lewis, *Chem. Rev.* **2010**, *110*, 6446.

[7] a) I. Roger, M. A. Shipman, M. D. Symes, *Nat. Rev. Chem.* **2017**, *1*, 0003; b) F. E. Osterloh, *Chem. Mater.* **2008**, *20*, 35; c) X. Zou, Z. Sun, Y. H. Hu, *J. Mater. Chem. A* **2020**, *8*, 21474.

[8] a) L. Wang, D. Mitoraj, S. Turner, O. V. Khavryuchenko, T. Jacob, R. K. Hocking, R. Beranek, *ACS Catal.* **2017**, *7*, 4759; b) M. N. Collomb, D. V. Morales, C. N. Astudillo, B. Dautreppe, J. Fortage, *Sustain. Energy Fuels* **2020**, *4*, 31; c) X. Fan, T. Wang, B. Gao, X. Xie, S. Zhang, X. Meng, H. Gong, Y. Guo, X. Huang, J. He, *Catal. Today* **2019**, *335*, 423.

[9] a) F. L. Li, Q. Shao, X. Huang, J. P. Lang, *Angew. Chem. Int. Ed.* **2018**, *57*, 1888; b) M. W. Louie, A. T. Bell, *J. Am. Chem. Soc.* **2013**, *135*, 12329; c) M. Ding, J. Chen, M. Jiang, X. Zhang, G. Wang, *J. Mater. Chem. A* **2019**, *7*, 14163; d) Y. Chi, W. Yang, Y. Xing, Y. Li, H. Pang, Q. Xu, *Nanoscale* **2020**, *12*, 10685.

[10] H. Furukawa, K. E. Cordova, M. O'Keeffe, O. M. Yaghi, *Science* **2013**, *341*, 1230444.

[11] a) S. Klaus, Y. Cai, M. W. Louie, L. Trotochaud, A. T. Bell, *J. Phys. Chem. C* **2015**, *119*, 7243; b) J. Du, F. Li, L. Sun, *Chem. Soc. Rev*. **2021**, *50*, 2663; c) B. J. Trześniewski, O. Diaz-Morales, D. A. Vermaas, A. Longo, W. Bras, M. T. M. Koper, W. A. Smith, *J. Am. Chem. Soc*. **2015**, *137*, 15112. d) C. Singh, I. Liberman, R. Shimoni, R. Ifraemov, I. Hod, *J. Phys. Chem. Lett.* **2019**, *10*, 3630.

[12] a) Y. Z. Chen, C. Wang, Z. Y. Wu, Y. Xiong, Q. Xu, S. H. Yu, H. L. Jiang, *Adv. Mater.* **2015**, *27*, 5010; b) S. Zhao, Y. Wang, J. Dong, C. T. He, H. Yin, P. An, K. Zhao, X. Zhang, C. Gao, L. Zhang, J. Lv, J. Wang, J. Zhang, A. M. Khattak, N. A. Khan, Z. Wei, J. Zhang, S. Liu, H. Zhao, Z. Tang,

Nat. Energy **2016**, *1*, 16184; c) M. Xie, Y. Ma, D. Lin, C. Xu, F. Xie, W. Zeng, *Nanoscale* **2020**, *12*, 67; d) W. He, H. M. Gao, R. Shimoni, Z. Y. Lu, I. Hod, *ACS Appl. Energy Mater.* **2019**, *2*, 2138.

[13] a) F. Sun, G. Wang, Y. Ding, C. Wang, B. Yuan, Y. Lin, *Adv. Energy Mater.* **2018**, *8*, 1800584; b) F. L. Li, P. Wang, X. Huang, D. J. Young, H. F. Wang, P. Braunstein, J. P. Lang, *Angew. Chem. Int. Ed.* **2019**, *58*, 7051; c) X. Zhao, P. Pachfule, S. Li, J. R. J. Simke, J. Schmidt, A. Thomas, *Angew. Chem. Int. Ed.* **2018**, *57*, 8921.

[14] G. Peng, M. Volokh, J. Tzadikov, J. Sun, M. Shalom, *Adv. Energy Mater.* **2018**, *8*, 1800566.

[15] C. Cao, D.-D. Ma, Q. Xu, X. T. Wu, Q. L. Zhu, *Adv. Energy Mater.* **2019**, *29*, 1807418.

[16] F. Dionigi, P. Strasser, *Adv. Energy Mater.* **2016**, *6*, 1600621.

[17] S. Y. Lim, S. Park, S. W. Im, H. Ha, H. Seo, K. T. Nam, *ACS Catal.* **2020**, *10*, 235.

[18] L. Bai, S. Lee, X. Hu, *Angew. Chem. Int. Ed.* **2020**, *59*, 2.

[19] a) K. Rui, G. Zhao, Y. Chen, Y. Lin, Q. Zhou, J. Chen, J. Zhu, W. Sun, W. Huang, S. X. Dou, *Adv. Funct. Mater.* **2018**, *28*, 1801554; b) c) N. Weidler, J. Schuch, F. Knaus, P. Stenner, S. Hoch, A. Maljusch, R. Schäfer, B. Kaiser, W. Jaegermann, *J. Phys. Chem. C* **2017**, *121*, 6455; c) W. He, H.-M. Gao, R. Shimoni, Z. Y. Lu, I. Hod, *ACS Appl. Energy Mater.* **2019**, *2*, 2138.

[20] L. Wang, Y. Wu, R. Cao, L. Ren, M. Chen, X. Feng, J. Zhou, B. Wang, *ACS Appl. Mater. Interfaces* **2016**, *8*, 16736.

[21] K. Li, Y. Zhang, Y. Z. Lin, K. Wang, F. T. Liu, *ACS Appl. Mater. Interfaces* **2019**, *11*, 28918.

[22] H. Zhang, W. Tian, X. Guo, L. Zhou, H. Sun, M. O. Tadé, S. Wang, *ACS Appl. Mater. Interfaces* **2016**, *8*, 35203.

[23] G. Peng, J. Qin, M. Volokh, C. Liu, M. Shalom, *J. Mater. Chem. A* **2019**, *7*, 11718.

[24] a) E. Tsuji, A. Imanishi, K. i. Fukui, Y. Nakato, *Electrochim. Acta* **2011**, *56*, 2009; b) J. M. Spurgeon, J. M. Velazquez, M. T. McDowell, *Phys. Chem. Chem. Phys.* **2014**, *16*, 3623; c) K. H. Ye, H. Li, D. Huang, S. Xiao, W. Qiu, M. Li, Y. Hu, W. Mai, H. Ji, S. Yang, *Nat. Commun.* **2019**, *10*, 3687.

[25] a) L. Francàs, S. Corby, S. Selim, D. Lee, C. A. Mesa, R. Godin, E. Pastor, I. E. L. Stephens, K.-S. Choi, J. R. Durrant, *Nat. Commun*. **2019**, *10*, 5208; b) L. Trotochaud, S. L. Young, J. K. Ranney, S. W. Boettcher, *J. Am. Chem. Soc.* **2014**, *136*, 6744.

[26] M. W. Louie, A. T. Bell, *J. Am. Chem. Soc*. **2013**, *135*, 12329.

[27] D. Klotz, D. A. Grave, A. Rothschild, *Phys. Chem. Chem. Phys.* **2017**, *19*, 20383.

[28] J. Hong, C. Chen, F. E. Bedoya, G. H. Kelsall, D. O'Hare, C. Petit, *Catal. Sci. Technol.* **2016**, *6*, 5042.

[29] a) C. Cao, D. D. Ma, Q. Xu, X. T. Wu, Q. L. Zhu, *Adv. Funct. Mater.* **2019**, *29*, 1807418; b) F. Zheng, D. Xiang, P. Li, Z. Zhang, C. Du, Z. Zhuang, X. Li, W. Chen, *ACS Sustain. Chem. Eng.* **2019**, *7*, 9743.

[30] D. Cardenas-Morcoso, R. Ifraemov, M. García-Tecedor, I. Liberman, S. Gimenez, I. Hod, *J. Mater. Chem. A* **2019**, *7*, 11143.

[31] R. Godin, Y. Wang, M. A. Zwijnenburg, J. Tang, J. R. Durrant, *J. Am. Chem. Soc.* **2017**, *139*, 5216.

[32] J. Liu, D. Zhu, C. Guo, A. Vasileff, S. Z. Qiao, *Adv. Energy Mater.* **2017**, *7*, 1700518.

[33] I. Liberman, W. He, R. Shimoni, R. Ifraemov, I. Hod, *Chem. Sci.* **2020**, *11*, 180.

[34] a) X. F. Chuah, C. T. Hsieh, C. L. Huang, D. Senthil Raja, H. W. Lin, S. Y. Lu, *ACS Appl. Energy Mater.* **2019**, *2*, 743. b) L. Trotochaud, J. K. Ranney, K. N. Williams, S. W. Boettcher, *J. Am. Chem. Soc.* **2012**, *134*, 17253.

Table of contents

Here we show carbon nitride (CN) photoanode with $NiFeO_xH_y$ as a cocatalyst with state-of-art photoelectrochemical performance thanks to superb water oxidation kinetics (reaching 85% faradaic efficiency for oxygen evolution), hole extraction properties, low onset potential, and good long-term stability (up to 35 h). Our findings position CN-based materials as cheap, efficient, and stable photoanode active layers for water-splitting photoelectrochemical cells.

Neeta Karjule, Chanderpratap Singh, Jesús Barrio, Jonathan Tzadikov, Itamar Liberman, Michael Volokh, Emilio Palomares, Idan Hod and Menny Shalom**

Carbon Nitride-Based Photoanode with Enhanced Photostability and Water Oxidation Kinetics

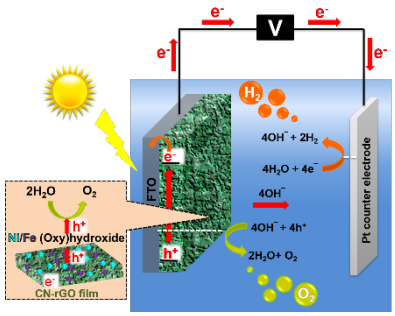

Carbon Nitride-Based Photoanode with Enhanced Photostability and Water Oxidation Kinetics

Neeta Karjule,[a] Chanderpratap Singh,[a] Jesús Barrio,[a] Jonathan Tzadikov,[a] Itamar Liberman,[a] Michael Volokh,[a] Emilio Palomares,[b] Idan Hod[a] and Menny Shalom[a]**

[a]Department of Chemistry and Ilse Katz Institute for Nanoscale Science and Technology, Ben-Gurion University of the Negev, Beer-Sheva 8410501, Israel

[b]Institute of Chemical Research of Catalonia, The Barcelona Institute of Science and Technology (ICIQ-BIST), E-43007 Tarragona, Spain; Catalan Institution for Research and Advanced Studies, E-08010 Barcelona, Spain

* Corresponding author:

Email: mennysh@bgu.ac.il, hodi@bgu.ac.il

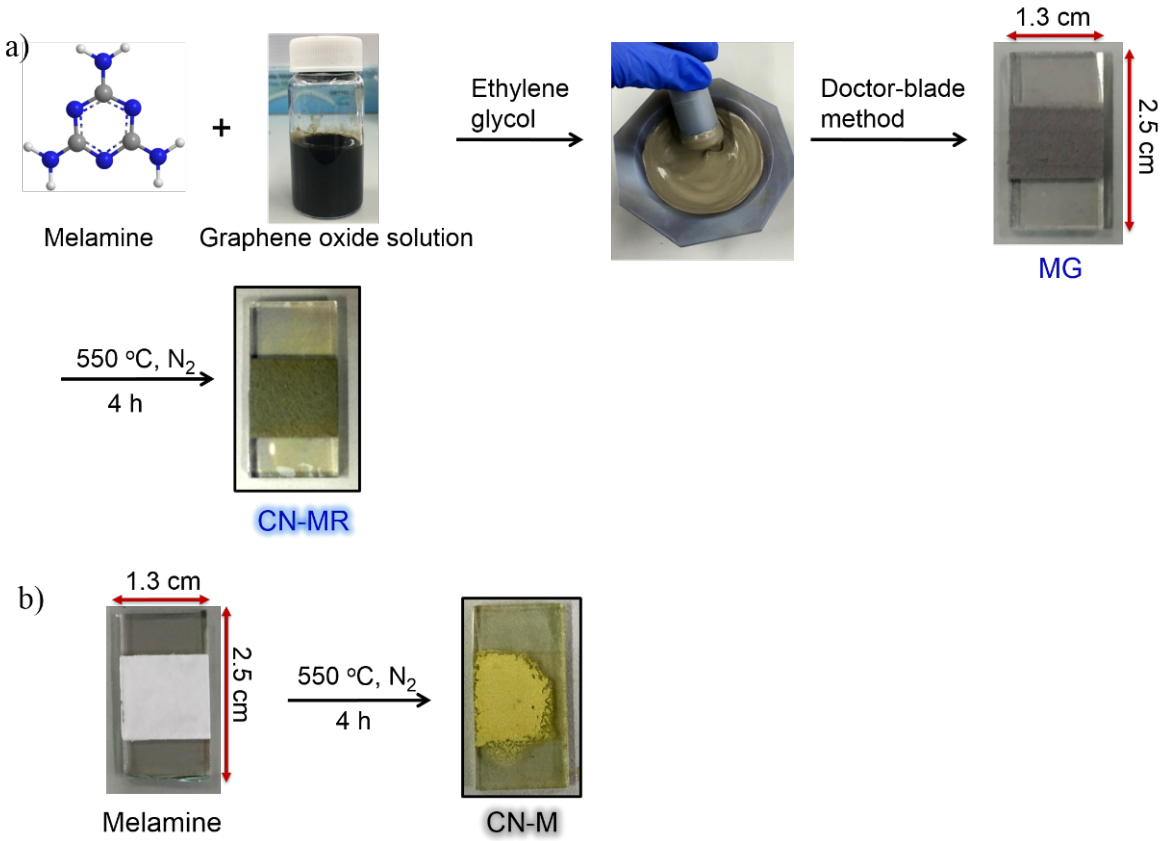

Figure S1. Electrode fabrication schemes. a) Melamine-graphene oxide (MG) and b) Melamine paste in ethylene glycol followed by electrode making using doctor-blade method on FTO (*L* (scotch tape layers) = 2). (YouTube video link explaining the doctor-blade method: https://www.youtube.com/watch?v=v9va5WENUQw)

The growth of homogeneous films on fluorine-doped tin oxide-coated glass (FTO, size: 1.3 cm × 2.5 cm) electrodes is shown in Figure S1. First, melamine (M) and graphene oxide (G) were ground in ethylene glycol to form a viscous paste,[1] which was then deposited on FTO to obtain MG films, followed by calcination at 550 °C under N_2 flow for 4 h to get CN-MR photoanodes. The melamine films were similarly prepared by grinding melamine powder in ethylene glycol followed by calcination.

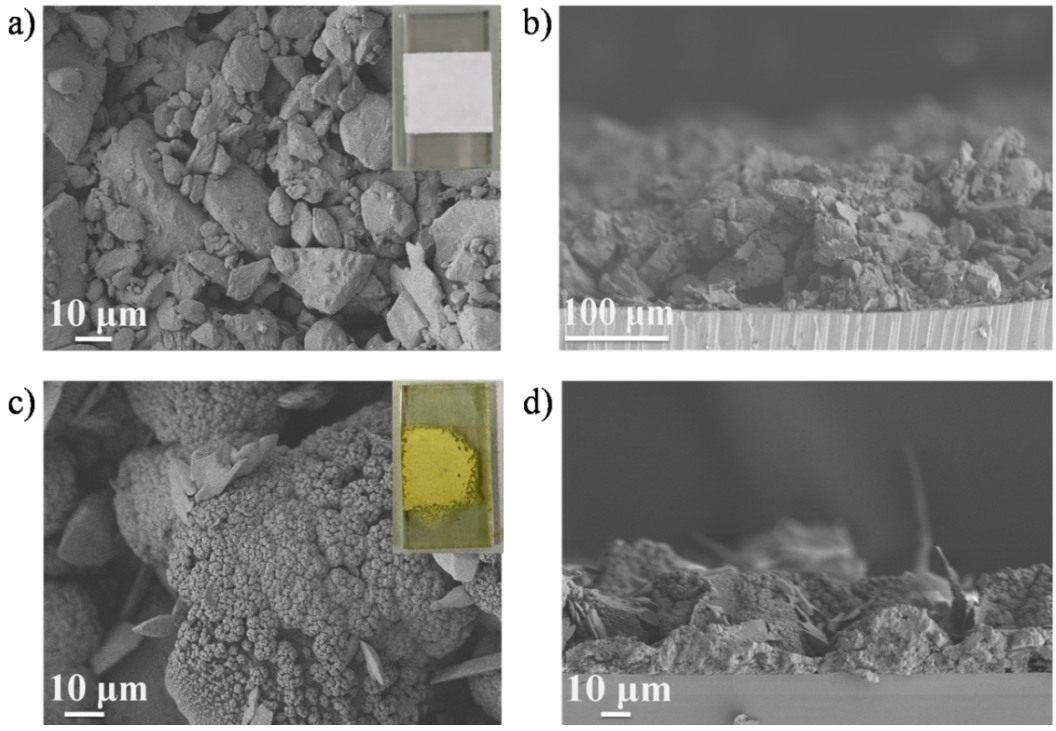

Figure S2. SEM characterization of melamine-based electrodes preparation. a) Top-view and b) cross-section of melamine film on FTO. c) Top-view and d) cross-section of CN-M on FTO (after calcination).

A cross-section SEM image of the melamine film shows the formation of a thick (*ca.* 130 µm) layer of melamine on the FTO (Figure S2b). CN-M electrodes exhibit an irregular CN layer over the FTO electrodes with a thickness of ~27 µm (Figure S2d).

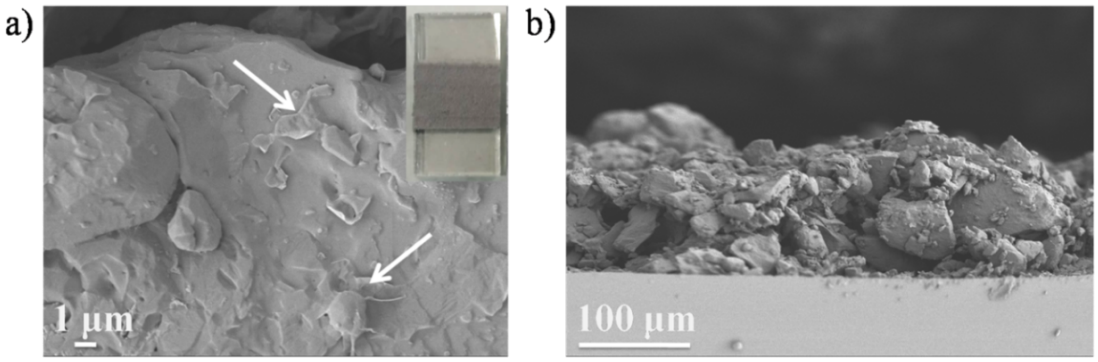

Figure S3. SEM characterization of melamine and GO-based electrodes. a) Top-view and b) cross-section of MG film on FTO.

The top-view SEM image shows the GO sheets forms bridges between the melamine aggregates. SEM images of FTO with MG film shows the formation of a thick (*ca.* 125 µm) layer (Figure S3b). The film thickness was further confirmed by measuring using a 3D laser confocal scanning microscope (see Figures S4 and S6).

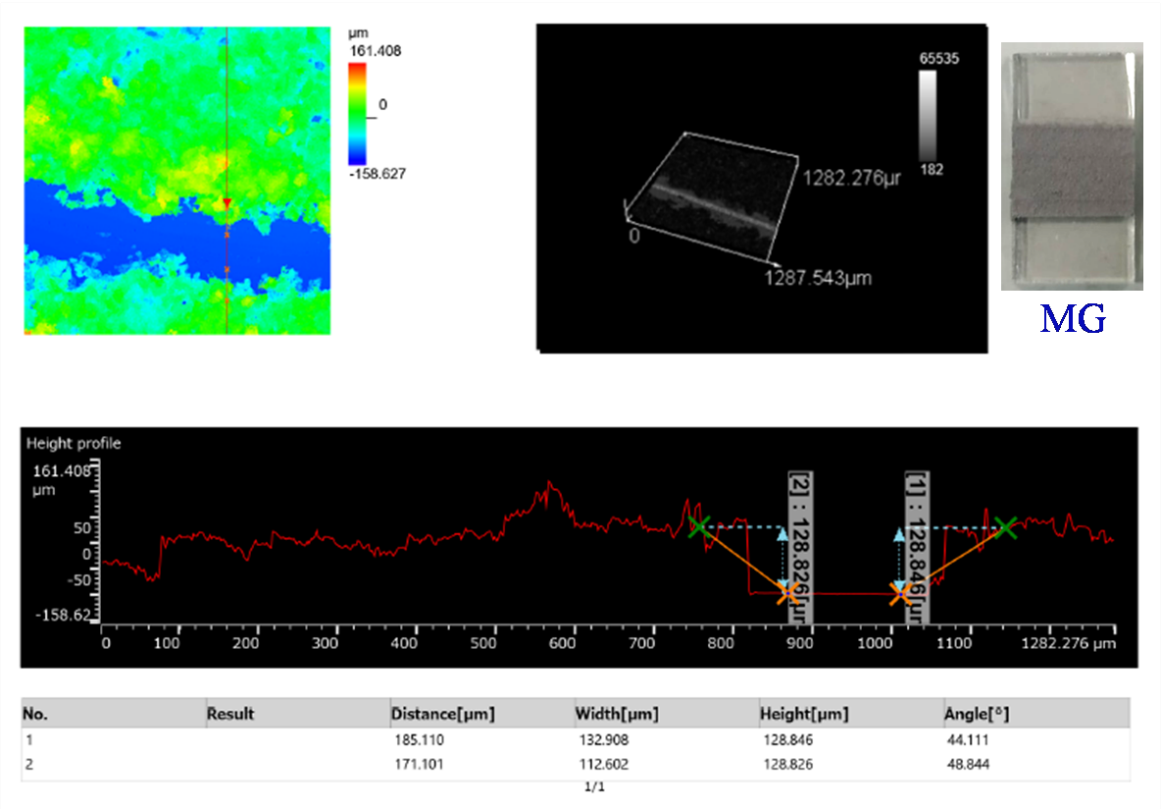

No.	Result	Distance[µm]	Width[µm]	Height[µm]	Angle[°]
1		185.110	132.908	128.846	44.111
2		171.101	112.602	128.826	48.844

1/1

Figure S4. Surface profile of MG electrodes for thickness measurement.

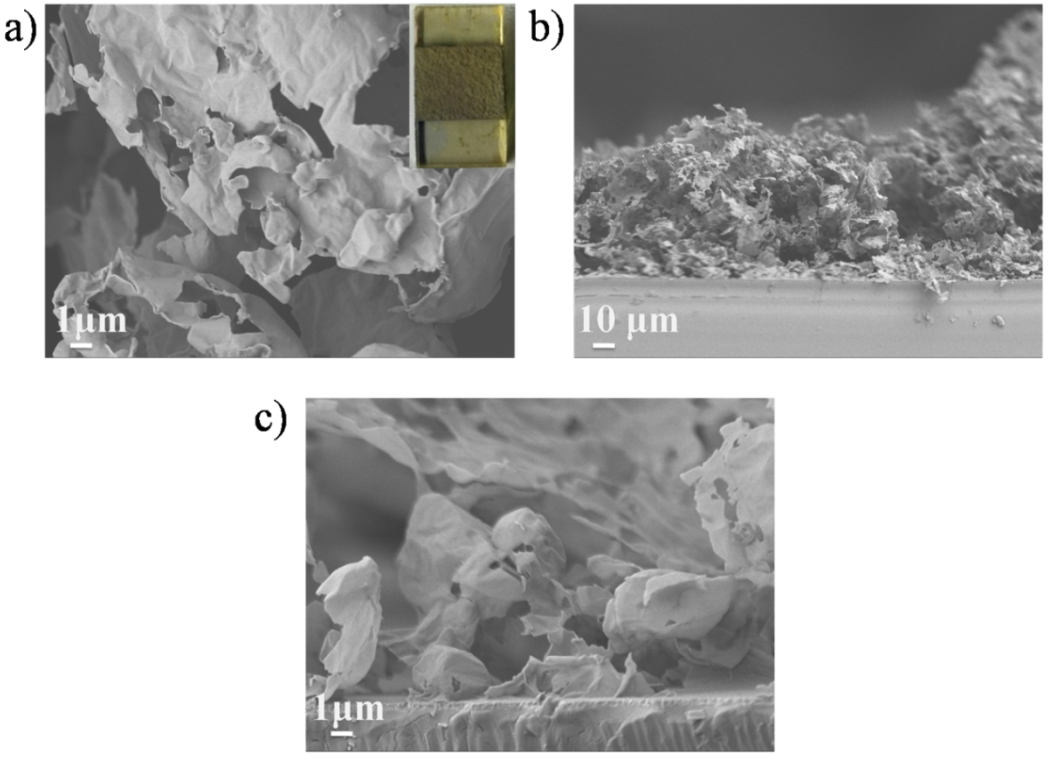

Figure S5. SEM characterization of CN-MR electrodes. a) Top-view, b) cross-section (~100 µm), and c) cross-section of CN-MR electrode close to the FTO's surface, showing intimate contact of CN with FTO.

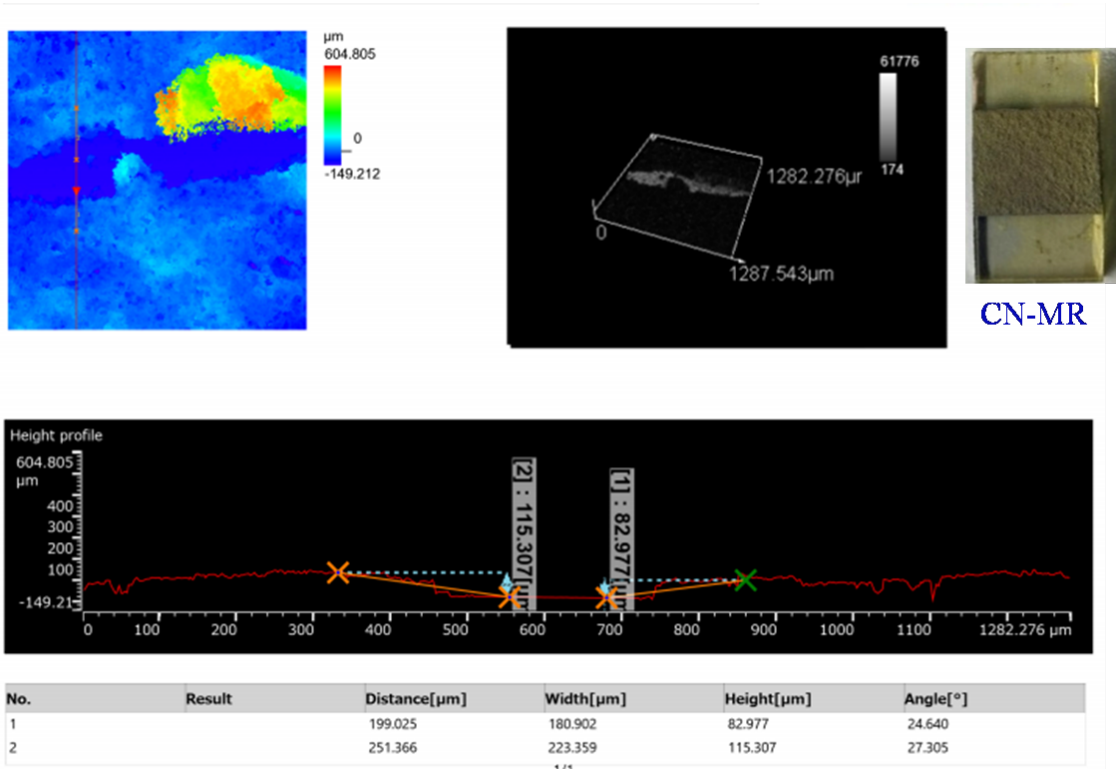

No.	Result	Distance[µm]	Width[µm]	Height[µm]	Angle[°]
1		199.025	180.902	82.977	24.640
2		251.366	223.359	115.307	27.305

Figure S6. Surface profile of CN-MR electrodes for thickness measurement.

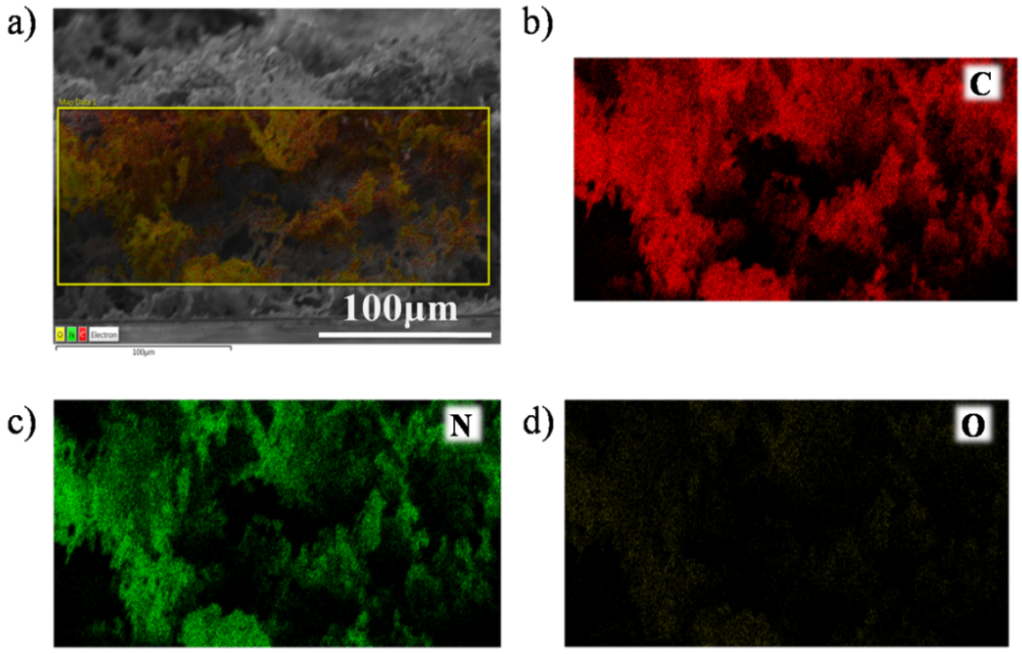

Figure S7. Cross-section SEM view and EDS of CN-MR. a) SEM image with overlaid elemental EDS mapping. Separate element distribution maps of b) carbon (red), c) nitrogen (green), and d) oxygen (yellow).

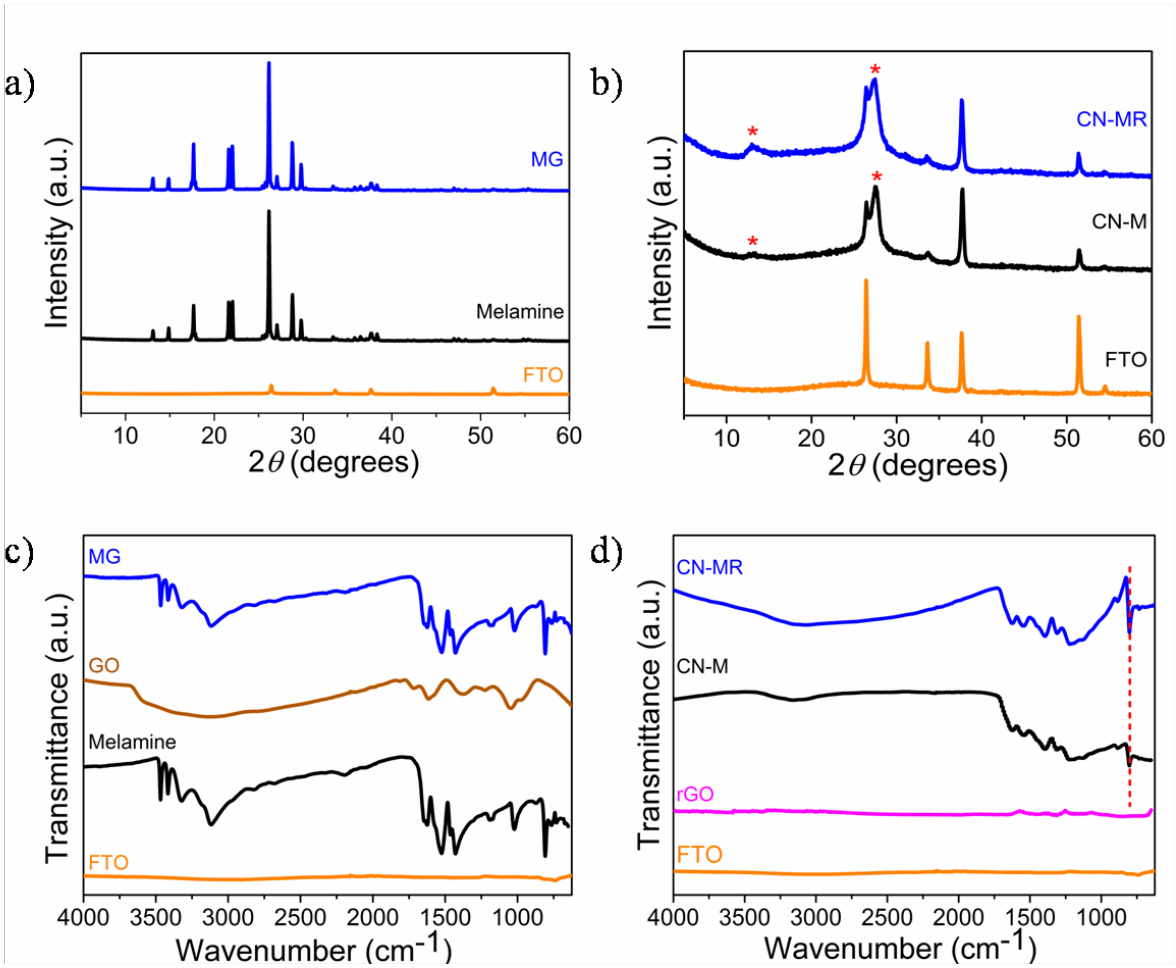

Figure S8. XRD and FTIR analysis. XRD patterns of films on FTO: a) before calcination and b) after calcination (red asterisks in panel (b) indicate crystal planes of graphitic carbon nitride). FTIR spectra of films on FTO: c) before calcination and d) after calcination.

FTIR and XRD of the CN films display similar characteristics of typical CN. In XRD, the two diffraction signals at 2θ values of 13.13° and 27.41° match well with the (100) and (002) crystal planes of graphitic carbon nitride (Figure S8b).[2] The red asterisks in panel (b) indicate crystal planes of graphitic carbon nitride. In the FTIR spectra of CN films, the broad peak around 3130 cm^{-1} belongs to free amine groups at the surface, the stretching bands of the CN heterocycles can be observed between 1200−1630 cm^{-1}, and the characteristic breathing mode of triazine rings appears at 805 cm^{-1} (Figure S8d). CN show a chemical structure like that of melon, in the form of linear polymers of heptazine linked by -N(H) groups forming sheets and presence of terminal NH_2 groups (Figure S9).[3] It is further supported by XPS analysis (Figure S10).

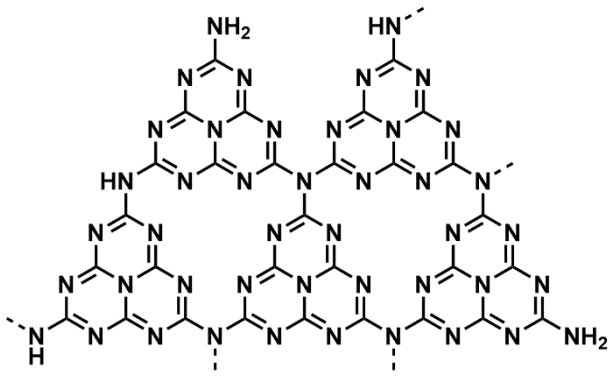

Figure S9. Proposed structure of CN showing chemical structure like melon.

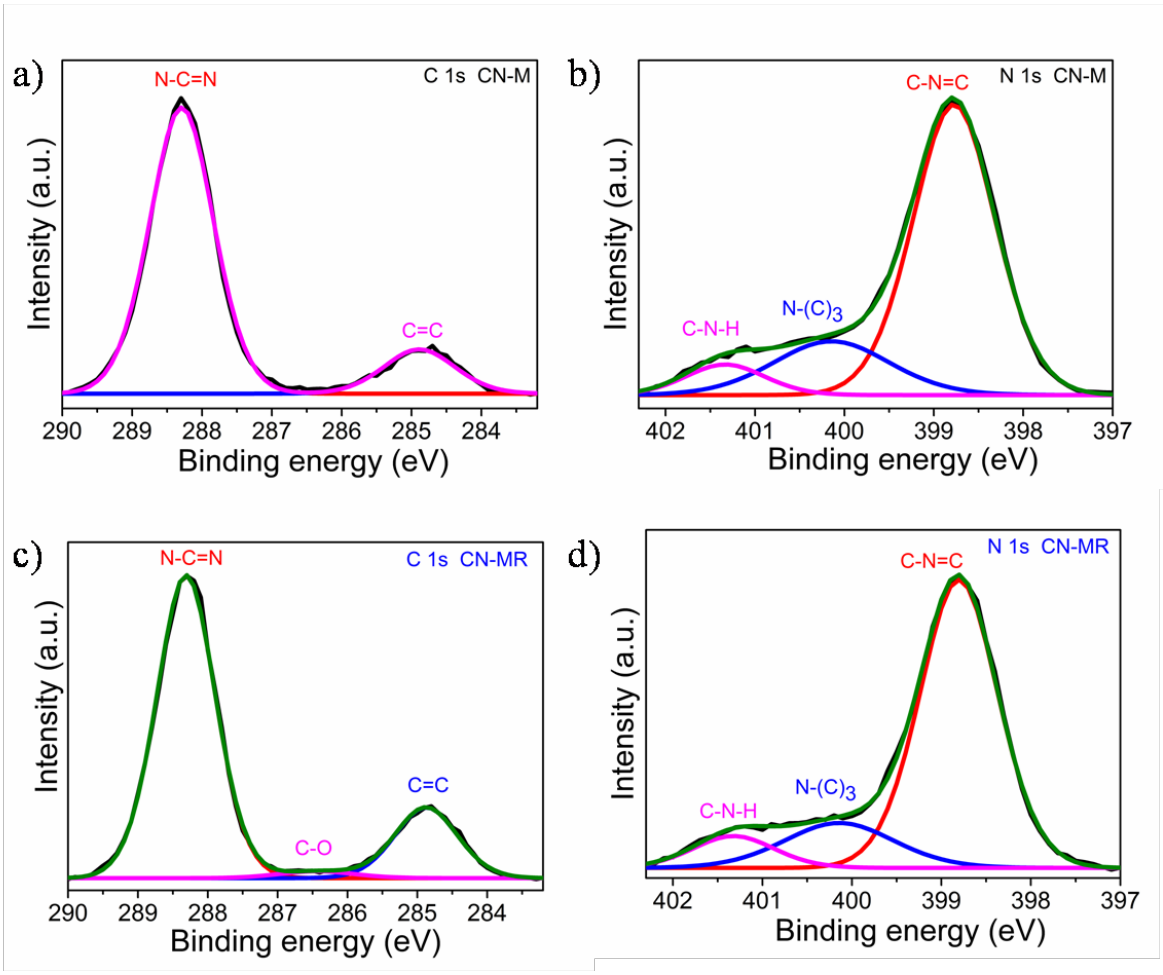

Figure S10. High-resolution XPS spectra of CN-M and CN-MR electrodes. a) C1s and b) N1s spectra of CN-M electrodes. High-resolution XPS spectra of of CN-MR electrodes: c) C1s and d) N1s. The experimental curve is presented in black; the fitted spectra are shown in green; the individual deconvoluted contributions in blue, red, and magenta.

The chemical states of CN-M and CN-MR films were investigated by XPS (Figure S10). In the C1s spectrum, the binding energies at 284.9 eV and 288.3 eV correspond to C–C bonds and C–N=C moieties, respectively. The peak at 286.4 eV, which was observed for CN-MR, belongs to C–O (surface-adsorbed atmospheric oxygen). The N1s spectrum displays three

peaks centered at 398.8, 400.2, and 401.4 eV, which are assigned to C–N=C bonds, tertiary nitrogen N−(C)$_3$ groups, and C–N–H bonds, respectively.

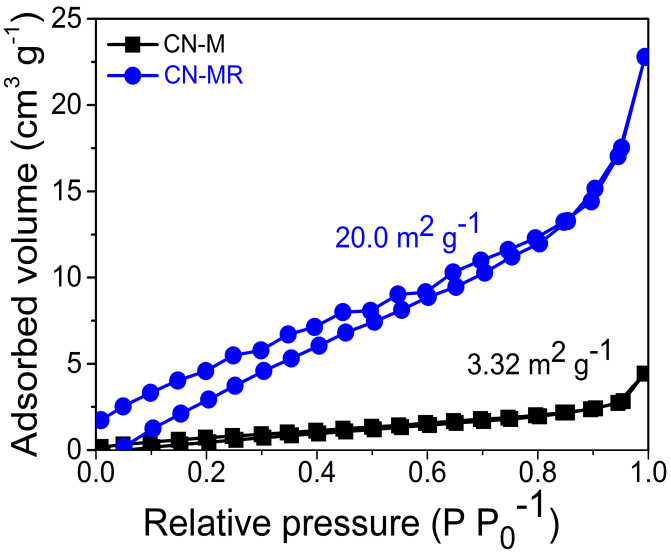

Figure S11. N_2 adsorption-desorption isotherms for CN-based electrodes (the actual experiments were performed by analyzing the relevant CN powder scratched from FTO). The values (3.32 and 20.0 m^2 g^{-1}) represent the specific surface area (CN-M and CN-MR, respectively), calculated using the BET model.

The N_2 sorption analysis in Figure S11 shows a six-fold enhancement of the specific surface area for CN-MR (S_A = 20.0 m^2 g^{-1}) relative to the pristine carbon nitride counterpart (CN-M, S_A = 3.32 m^2 g^{-1}).

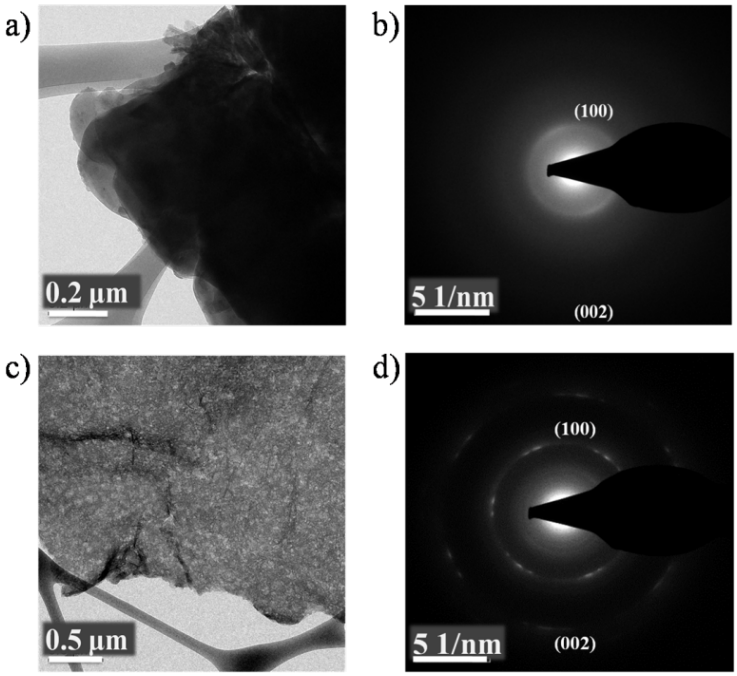

Figure S12. TEM analysis. a) TEM image of CN-M and b) the corresponding selected area electron diffraction (SAED). c) TEM image of CN-MR and d) the corresponding SAED.

As shown in Figure S12, CN-MR displays thinner and more crystalline nanosheets after incorporation of rGO in comparison with CN-M.

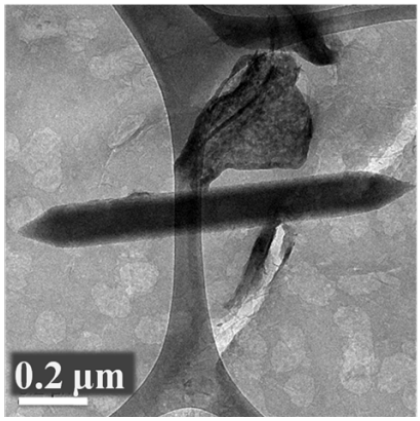

Figure S13. TEM image of CN-MR/MOF.

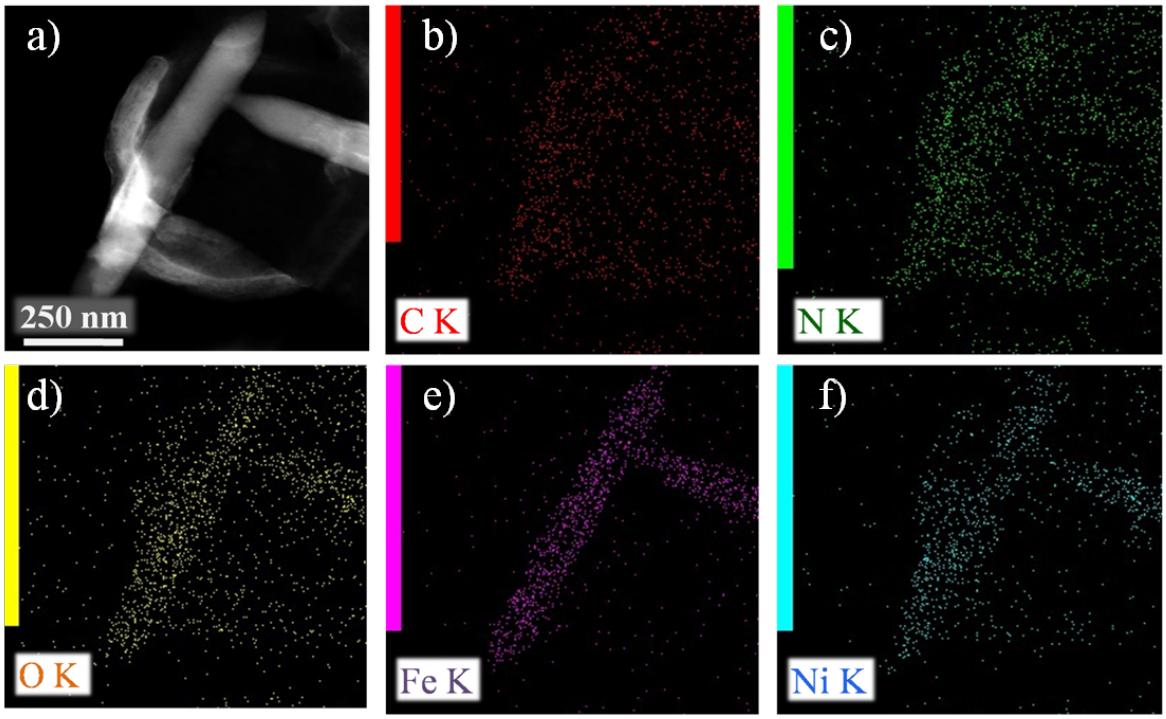

Figure S14. a) High-angle annular dark-field (HAADF)-STEM images CN-MR/MOF. EDS mapping showing the spatial distribution (K-edge signals) at this location of the following elements: b) carbon, c) nitrogen, d) oxygen, e) iron, and f) nickel.

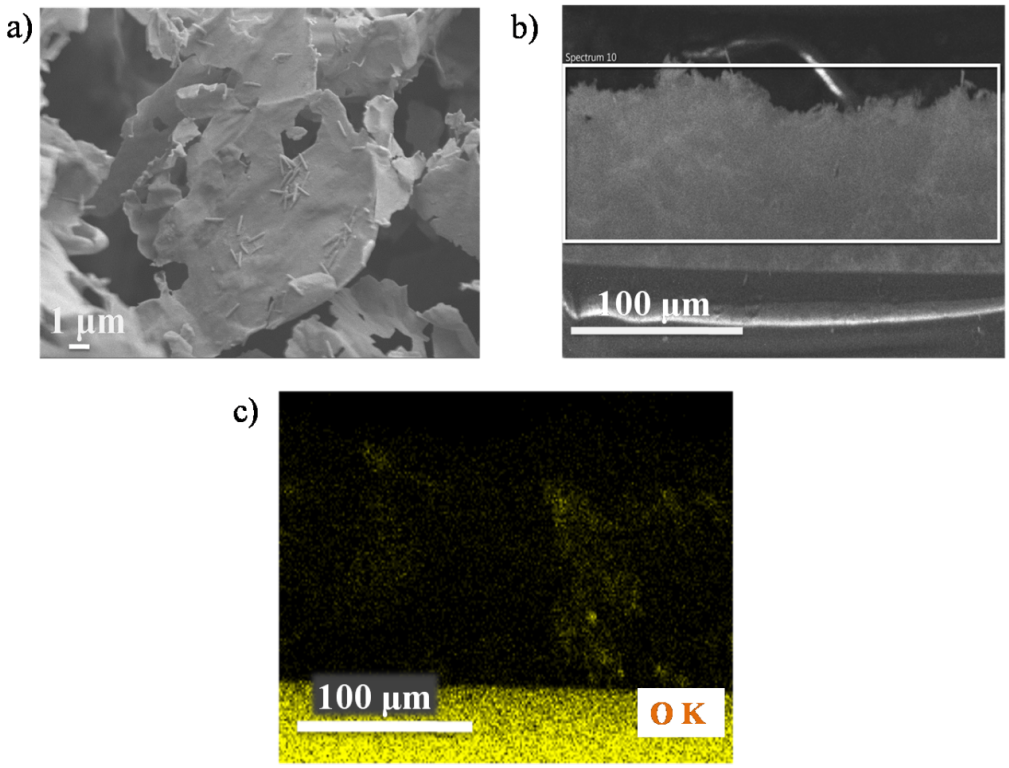

Figure S15. SEM and EDS analysis of CN-MR/MOF. a) Top-view, b) cross-section, and c) SEM-EDS mapping of CN-MR/MOF showing the elemental distribution of oxygen (O).

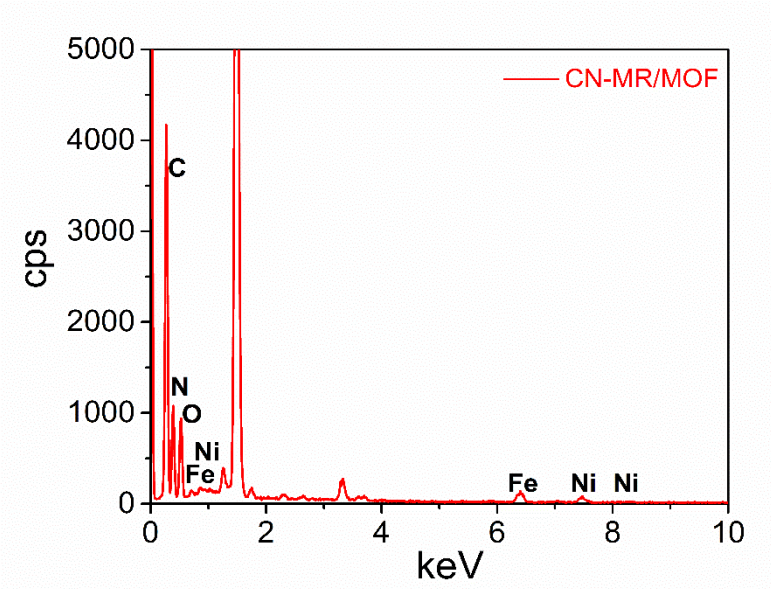

Figure S16. EDS spectrum of CN-MR/MOF films.

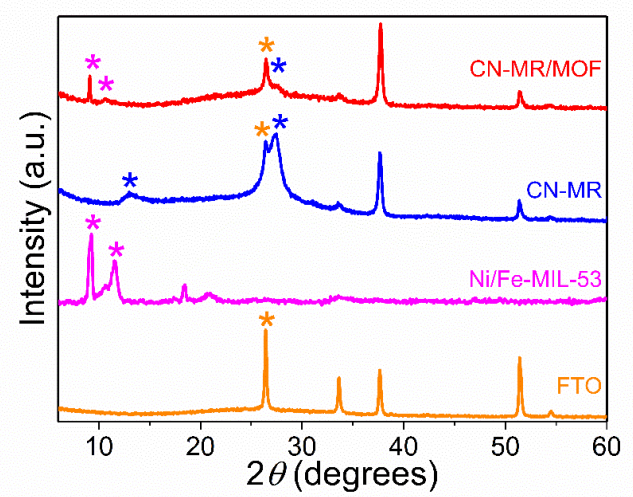

Figure S17. XRD patterns for MOF (Ni/Fe-MIL-53), CN-MR, and CN-MR/MOF on FTO substrates.

The formation of MOFs in CN films was confirmed by XRD patterns showing significant diffraction reflections at 9.12° and 10.6° (marked using pink asterisks), which match well with published reports (Figure S17).[4] The XRD patterns of CN-MR show two significant diffraction reflections at 13.13° and 27.41°, ascribed to the (100) and (002) planes of CN. The XRD measurements suggest that the CN-MR/MOF film on FTO has low crystallinity with less observable CN characteristic peaks, most likely due to strong signals from the FTO (marked using orange asterisks), which hinder the signal of the CN-MR.

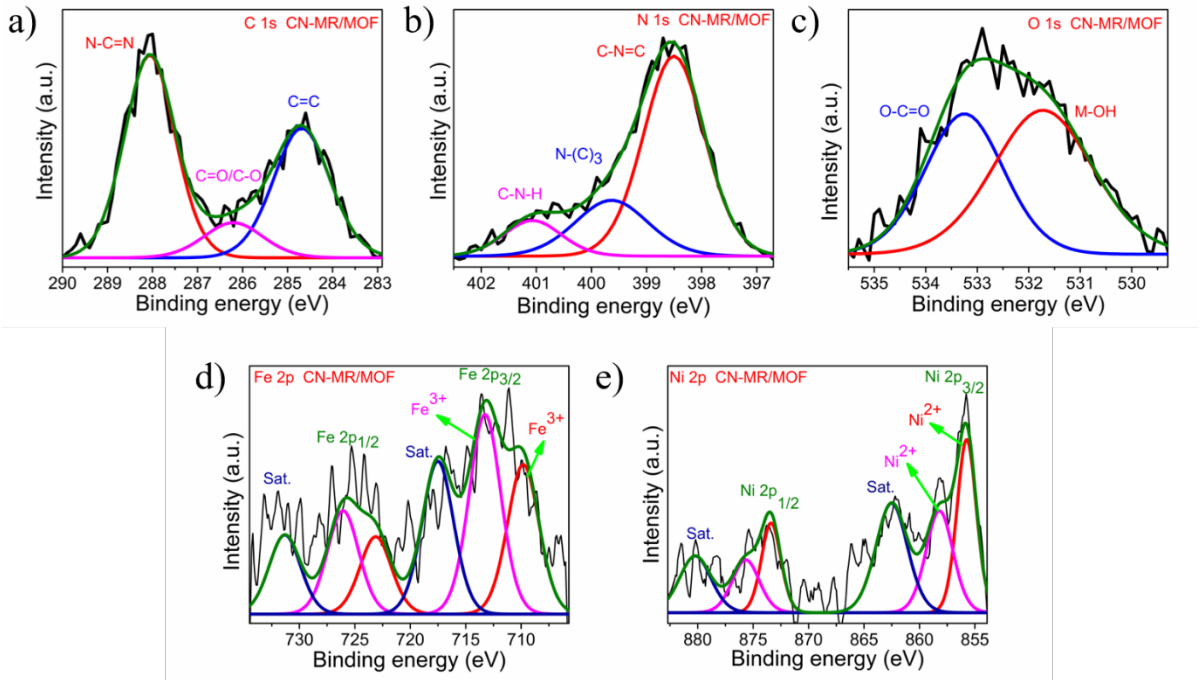

Figure S18. High-resolution XPS spectra of CN-MR/MOF for electrodes. a) C 1s, b) N 1s, c) O 1s, d) Fe 2p, and e) Ni 2p. Experimental spectra are plotted in black; green lines represent the fitted spectra; magenta, blue, and red are the individual deconvoluted fitted peaks.

XPS measurements were carried out to analyze the chemical composition and the surface electronic states of CN-MR/MOF films. As shown in Figure S18, XPS measurements show that the film consists of C, N, O, Fe, and Ni elements, thus confirming the successful synthesis of the desired MOF.[5] In the high-resolution C 1s spectra, the peaks at 284.7 and 288.1 eV can be assigned to the C−C bond and N−C=N in the triazine unit, respectively. The peak at 286.2 eV represents the C−O bond of carboxylate groups (O−C=O), originating from the BDC ligand. In the deconvoluted N 1s spectra, three peaks appear at 398.5, 399.7, and 401.1 eV, which are attributed to C–N=C bonds, tertiary nitrogen N−$(C)_3$ groups, and C–N–H bonds, respectively, confirming the heptazine building units of CN. The O 1s spectrum exhibits characteristic peaks at 531.7 and 533.2 eV, assigned to the metal hydroxides (M–OH) and O−C=O groups of BDC ligand, respectively.

High-resolution Ni 2p and Fe 2p spectra show $2p_{1/2}$ and $2p_{3/2}$ electronic configurations due to the spin–orbit splitting as shown in Figure S18d–e. In the Fe 2p spectrum, the binding energy peak around 713.2 eV is ascribed to Fe $2p_{3/2}$, and the peak around 725.6 eV is assigned to Fe $2p_{1/2}$, which are characteristic to the Fe^{3+} oxidation state (Figure S18d). The peak at 717.4 eV (Fe $2p_{3/2}$) and 731.3 eV (Fe $2p_{1/2}$) are Fe 2p satellite peaks. In general, the Fe $2p_{3/2}$ (or $2p_{1/2}$) and Ni $2p_{3/2}$ (or $2p_{1/2}$) spectra show a complex structure with intense satellite (Sat.) signals of high binding energy adjacent to the main peaks, which is ascribed to a multielectron excitation (shake-up peaks). The Ni 2p spectrum shows two typical peaks around 856 and 873.4 eV that are associated with Ni $2p_{3/2}$ and Ni $2p_{1/2}$ electronic configurations, respectively, which are characteristic of the Ni^{2+} oxidation state. Ni $2p_{3/2}$ can be further deconvoluted into two peaks at 855.7 and 858.2 eV, which correspond to two different Ni^{2+} coordination species (Ni^{2+}−X−Ni and Ni^{2+}−X−Fe, X = O, or BDC, respectively)[6]. Likewise, two corresponding satellite peaks at 862.5 and 880.2 eV, appear for Ni $2p_{3/2}$ and Ni $2p_{1/2}$ electronic configurations, respectively. Therefore, the XPS data analysis confirms the formation of bimetallic Ni/Fe-MIL-53 by solvothermal reaction in the CN-MR films.[4]

Table S1. Elemental analysis of CN-MR/MOF obtained by XPS depth profile measurements (measured at ~ 17.5 nm) and SEM-EDS mapping

Element	by XPS (at. %)	by EDS[a] (wt. %)	by EDS[a] (at. %)
C	44.2 (1s)	36.0 ± 0.5	41.8 ± 0.6
N	40.0 (1s)	38.0 ± 0.7	37.8 ± 0.7
O	9.9 (1s)	22.5 ± 0.5	19.6 ± 0.4
Fe	2.3 (2p)	2.0 ± 0.1	0.50 ± 0.03
Ni	3.7 (2p)	1.4 ± 0.1	0.34 ± 0.02

[a]all quantification using K-edge lines

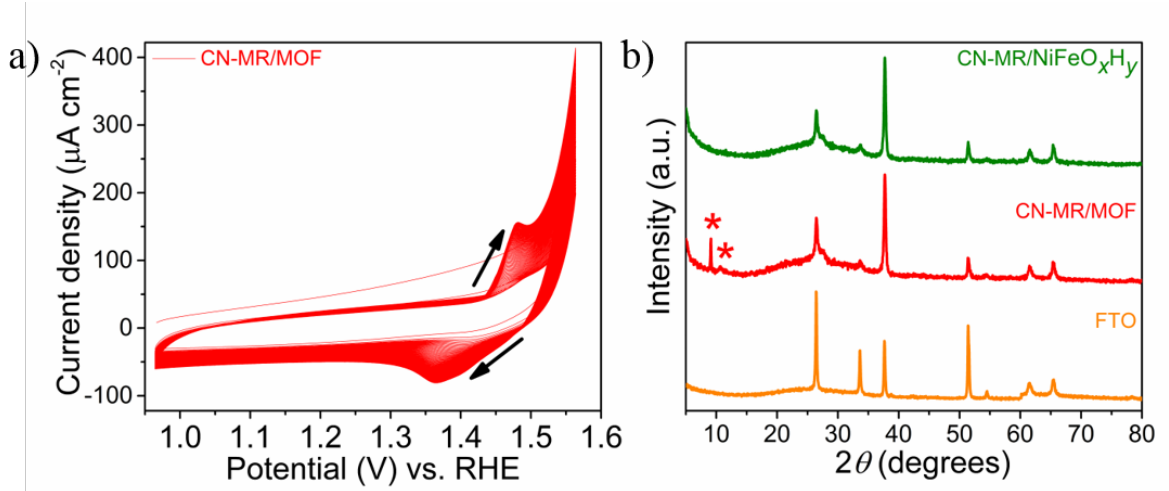

Figure S19. Cyclic voltammetry and its structural influence. a) Cyclic voltammograms of CN-MR/MOF in 0.1 M KOH (100 cycles) at a scan rate of 100 mV s^{-1} and b) XRD patterns of CN-MR/MOF before (red) and after CV (green) on FTO electrodes (pristine FTO substrate XRD pattern (orange) at the bottom). The red asterisks in panel (b) indicate characteristic MOF diffractions. The redox peaks of Fe^{3+}/Fe^{2+} are superimposed on the redox peaks of Ni^{3+}/Ni^{2+} as both occur in the potential range of 1.3–1.5 V *vs.* RHE.

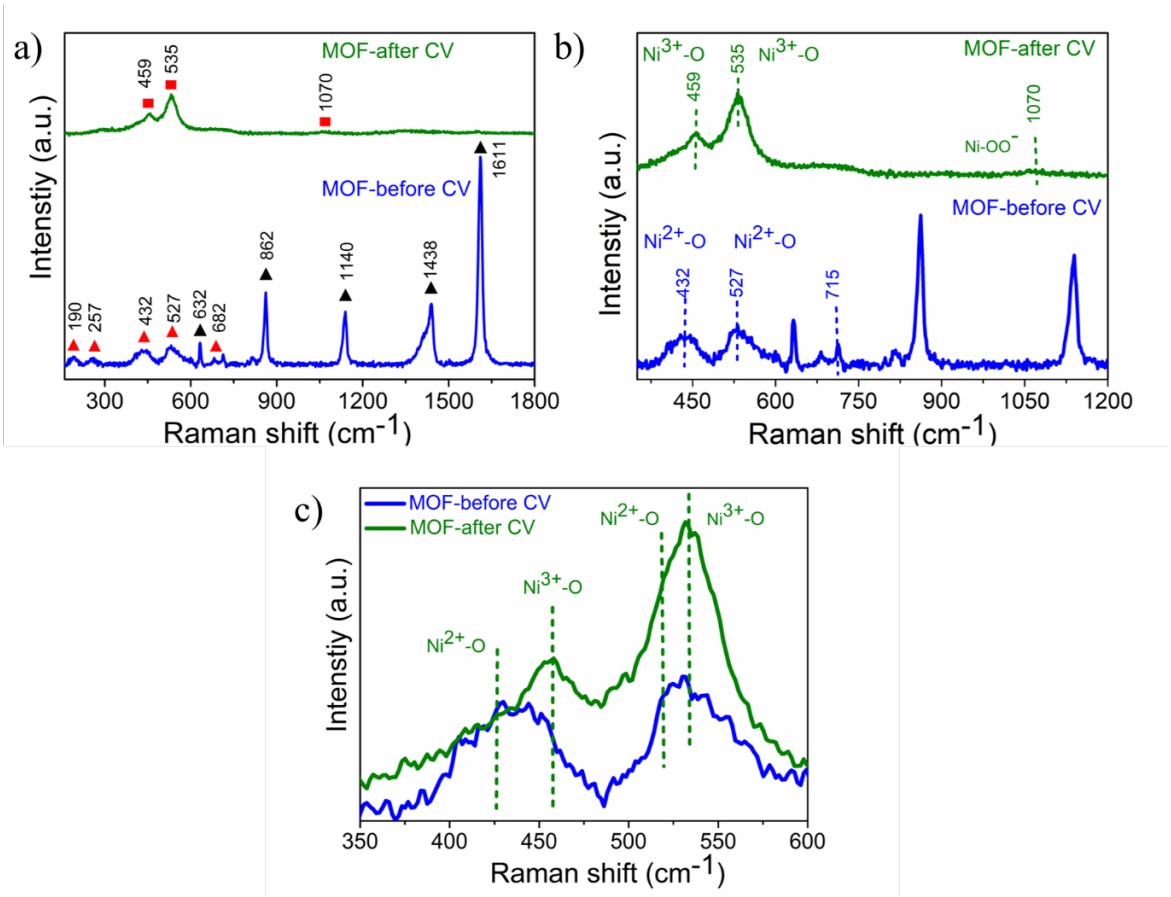

Figure S20. Raman spectra. a) MOF (Ni/Fe-MIL-53) before (blue) and after CV (green) on FTO electrodes, b) and c) Magnified areas of the Raman spectrum of MOF before and after CV, which is shown in (a).

In Figure S20a, the MOF exhibits two sets of Raman peaks: the red triangle belongs to the metal nodes of MIL-53, which is similar to the Raman signals of $Ni(OH)_2$ (432 cm^{-1})/$FeNiOH_x$ (527 and 682 cm^{-1}) whereas black triangle belongs to the organic ligands and/or the bonds of metal-ligands.[6] After electrochemical conversion ($NiFeO_xH_y$ formation), the set of black triangles were disappeared in the Raman spectra suggesting the BDC organic ligands is replaced by OH^-/O_2^-. The two strong Raman bands around 459 and 535 cm^{-1} were observed and correspond to the Ni–O bending (Ni^{3+}–O) and stretching vibrations of NiOOH (Ni^{3+}–O), respectively (Figure S20b). The existence of Ni^{2+}–O is evident from the shoulder around 425 and 519 cm^{-1} (Figure 20c).[7] A broad band in the range of 950 to 1100 cm^{-1} is attributed to Ni–OO^- (Figure 20b).

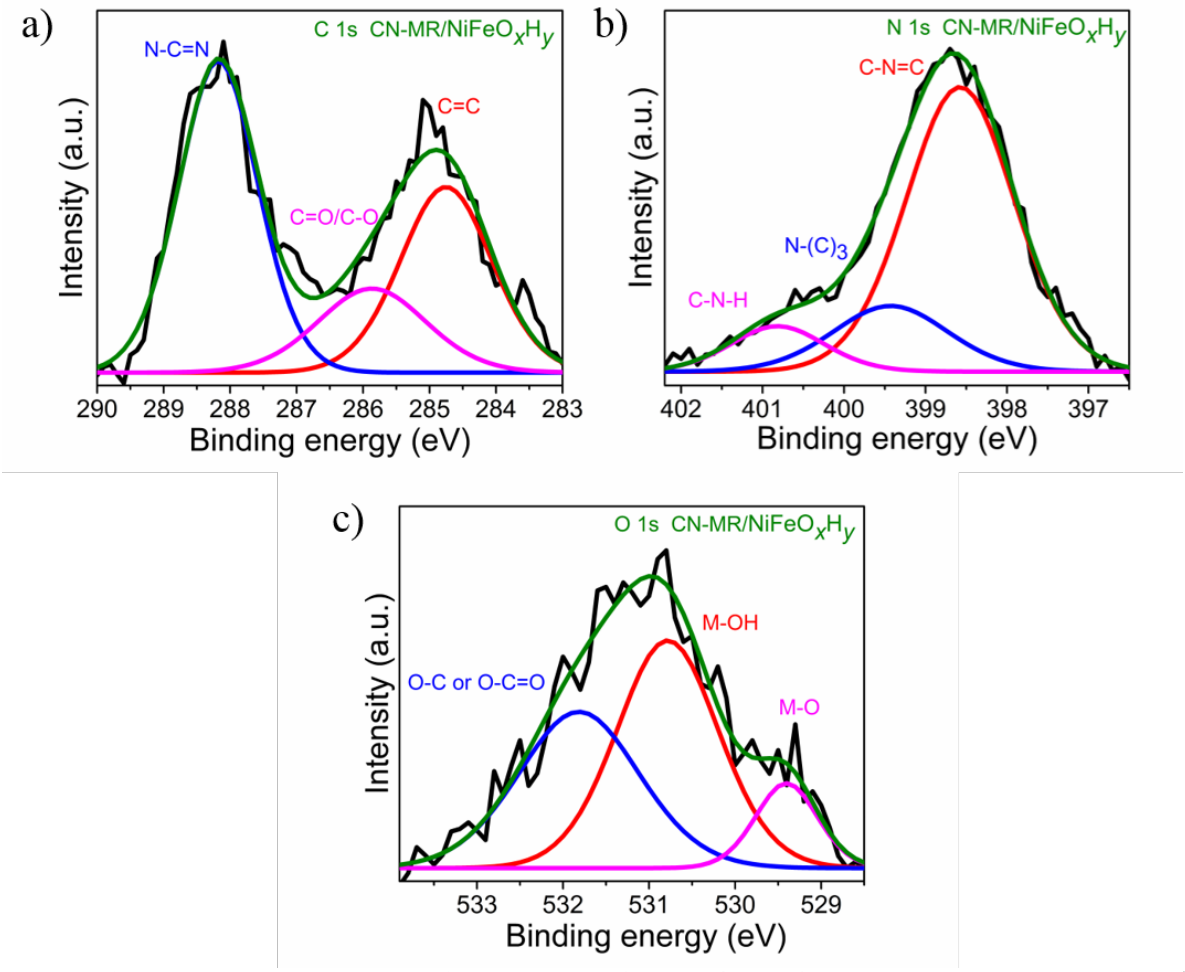

Figure S21. High-resolution XPS spectra of CN-MR/$NiFeO_xH_y$ electrodes (after CV). (a) C 1s, (b) N 1s, and (c) O 1s. Experimental spectra are plotted in black; green lines represent the fitted spectra; the magenta, blue, and red curves are the individual deconvoluted fitted peaks.

C1s and N1s after CV (Figure S21) show similar chemical composition for C and N elements for the CN framework as observed before CV (see Figure S10c–d).

Table S2. Elemental analysis of CN-MR/NiFeO$_x$H$_y$ (after CV) obtained by XPS depth profile measurements (measured at ~ 17.5 nm) and SEM-EDS mapping

Element	by XPS (at. %)	by EDS[a] (wt. %)	by EDS[a] (at. %)
C	45.58 (1s)	47.8 ± 0.7	54.4 ± 0.8
N	32.45 (1s)	24.6 ± 0.5	24.0 ± 0.5
O	18.09 (1s)	24.5 ± 0.5	20.9 ± 0.4
Fe	1.83 (2p)	1.7 ± 0.1	0.41 ± 0.02
Ni	2.06 (2p)	1.4 ± 0.1	0.32 ± 0.02

[a]all quantification using K-edge lines

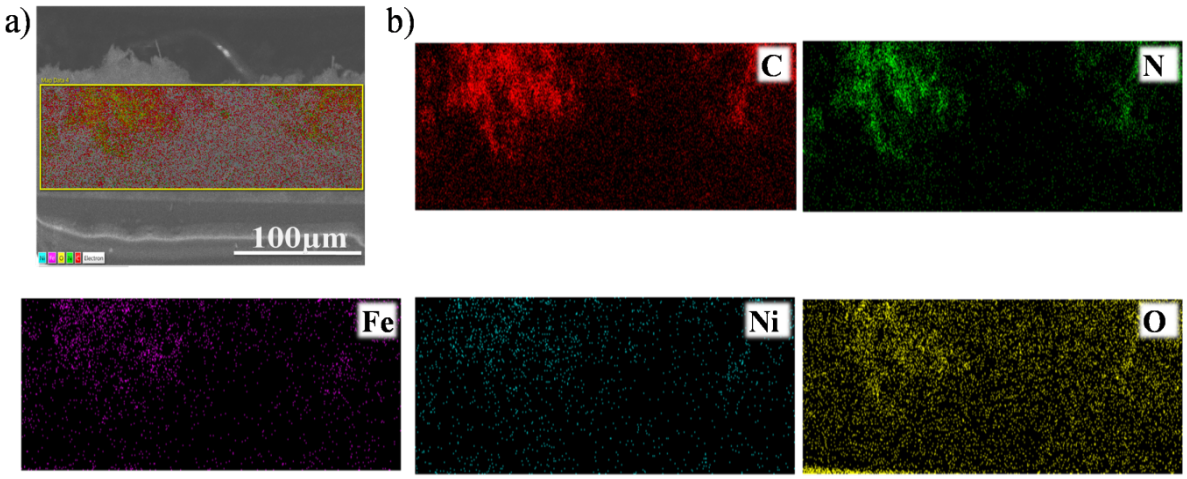

Figure S22. **Cross-section SEM view and EDS of CN-MR/NiFeO$_x$H$_y$ (after CV).** a) SEM image with overlaid elemental EDS mapping. b) Separate element distribution maps of carbon (red), nitrogen (green), iron (purple), nickel (cyan), and oxygen (yellow) confirming the NiFeO$_x$H$_y$ presence throughout the film thickness.

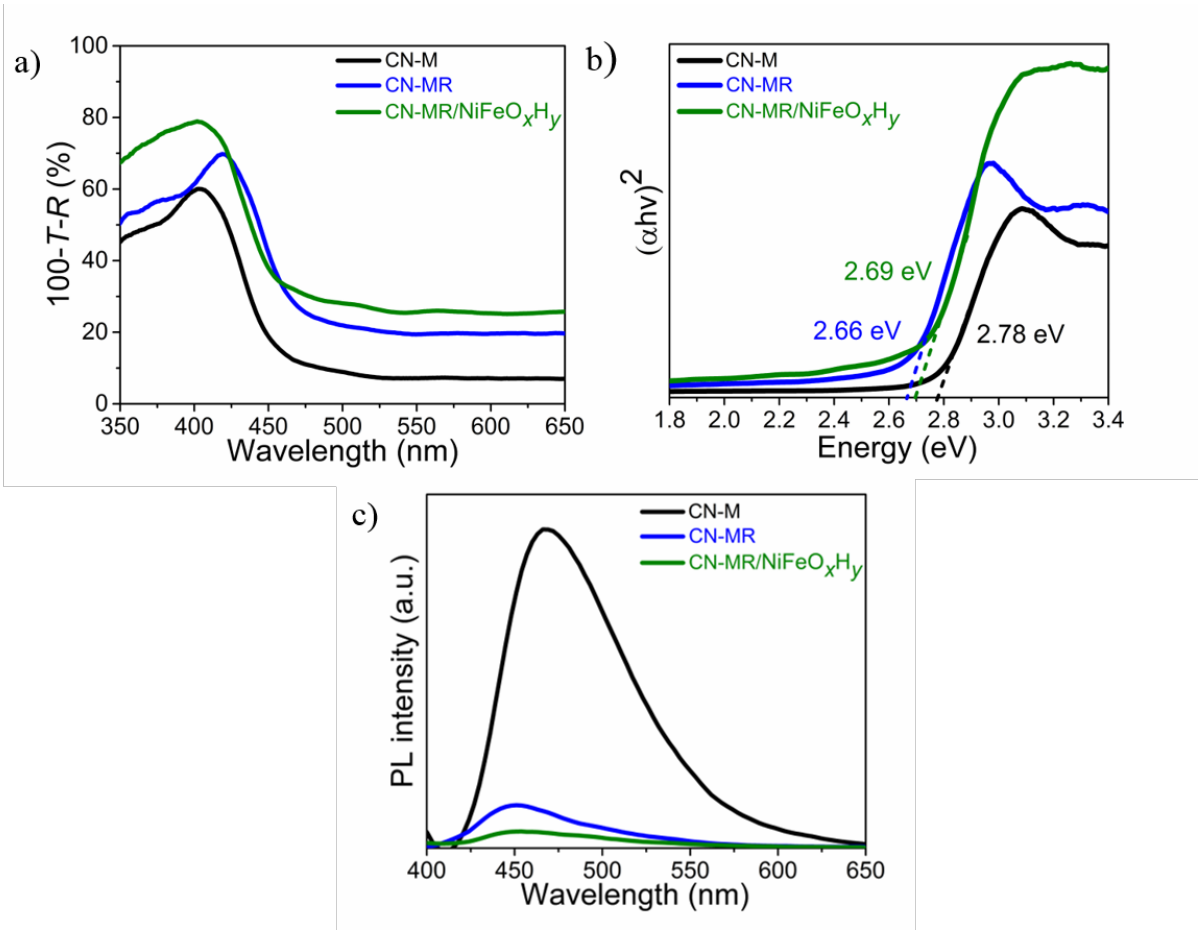

Figure S23. **Optical characterization of CN-based photoelectrodes.** a) UV–vis spectra of CN films on FTO, b) Tauc plot analysis assuming a direct band gap semiconductor, and c) photoluminescence (PL) spectra (excited at 370 nm) of CN-M (black), CN-MR (blue), and CN-MR/NiFeO$_x$H$_y$ (green) electrodes.

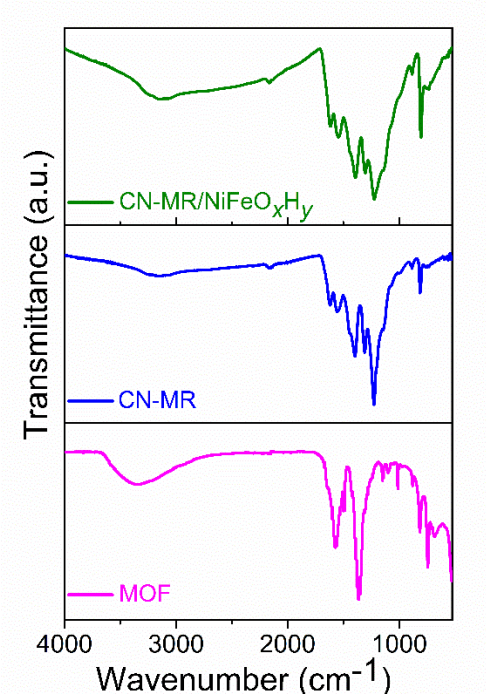

Figure S24. FTIR of MOF (Fe/Ni-MIL-53), CN-MR, and CN-MR/NiFeO$_x$H$_y$.

In the FTIR spectrum of MOF, the peaks at 3362, 1369, 1563, and 738 cm^{-1} can be attributed to the stretching vibrations of the O–H, symmetric and asymmetric vibrations of the carboxylate (O–C=O) groups, and the C–H bending vibrations of the benzene rings, respectively (Figure S24). In addition, the peaks at 531 cm^{-1} are assigned to Fe–O vibrations.[8] FTIR spectra of CN-MR/$NiFeO_xH_y$ indicate typical CN characteristics with a stronger and broader signal at 3158 cm^{-1} due to the presence of metal hydroxide (M–OH) species. CN-MR/$NiFeO_xH_y$ exhibits a sharp and intense band at 807 cm^{-1} that can be attributed to the vibration of triazine rings.

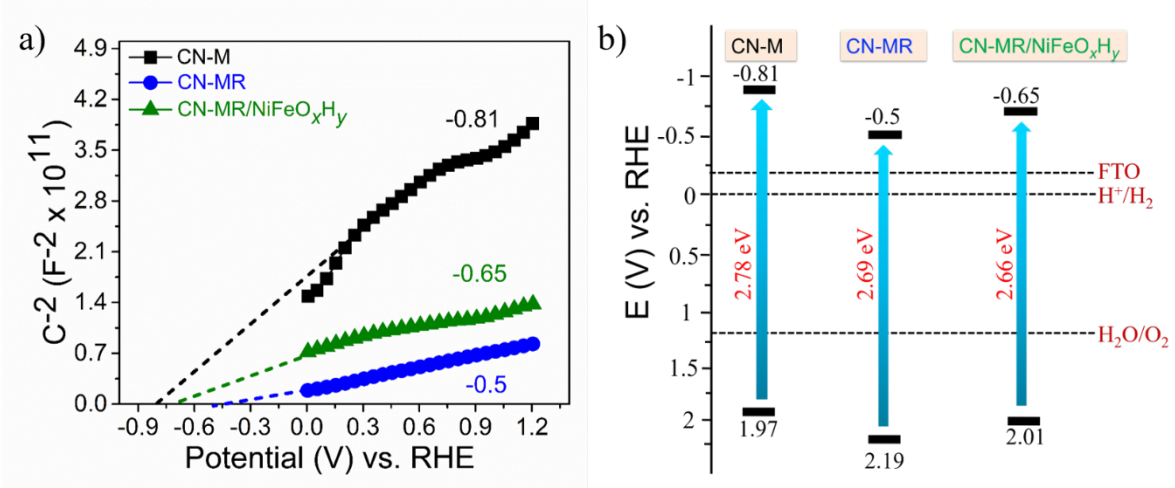

Figure S25. Energy level positions estimation using Mott-Schottky analysis. a) Mott-Schottky plots and (b) the corresponding proposed energy diagram of the CN electrodes determined from the optical E_g and the Mott-Schottky analysis (conduction band).

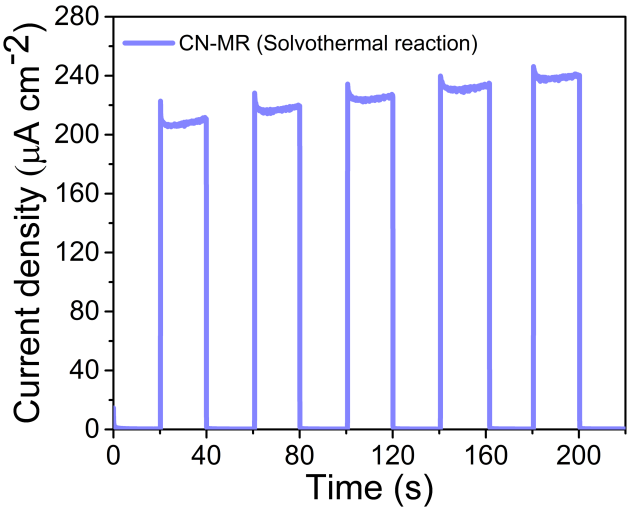

Figure S26. Photocurrent of CN-MR electrode (chronoamperometry at 1.23 V *vs.* RHE in 0.1 M KOH aqueous solution) that underwent a control experiment to verify that the catalytic improvement stems only from the MOF. The CN-MR electrode was subjected to the same solvothermal reaction conditions but without the MOF precursors.

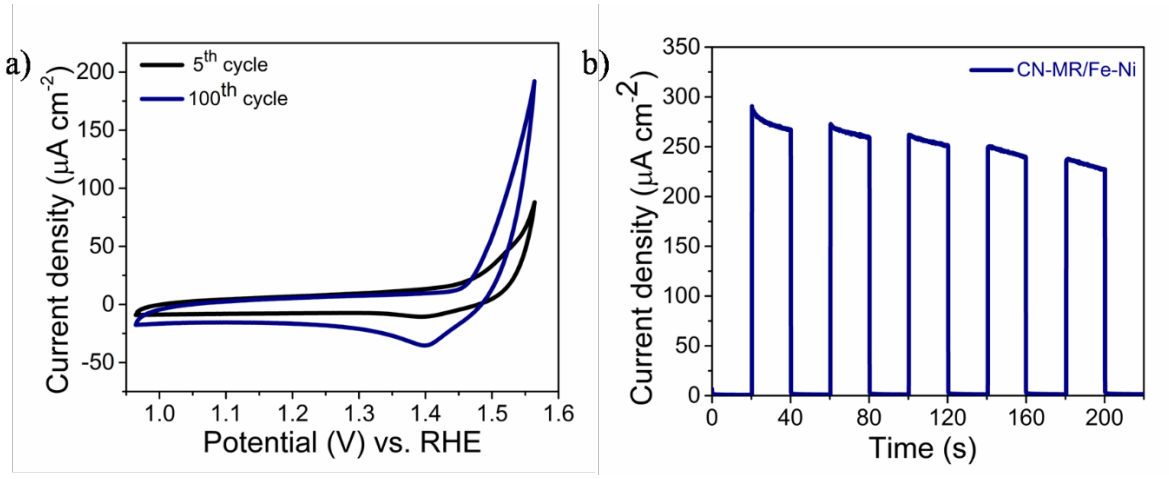

Figure S27. Electrochemical characterization of CN-MR/Fe-Ni without formed MOF. a) Cyclic voltammograms and b) chronoamperometry of CN-MR/Fe-Ni in 0.1 M KOH (the solvothermal synthesis was carried out on the CN-MR with Fe- and Ni-precursors but without BDC, preventing the MOF's formation.

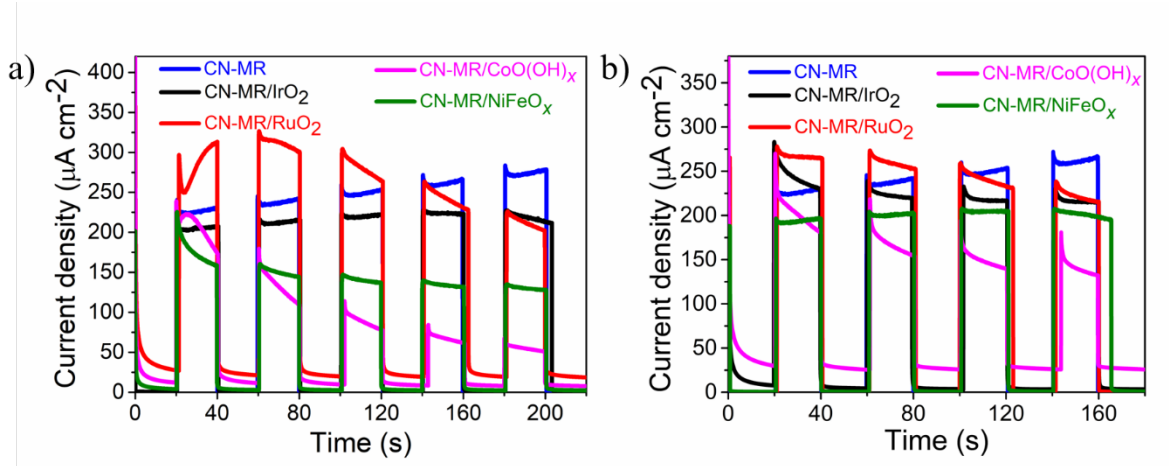

Figure S28. Chronoamperometric characterization of CN-MR electrodes containing different OER cocatalysts. Photocurrent densities measured at 1.23 V *vs.* RHE in a) 0.1 M KOH (pH 13.1) and b) 0.1 M phosphate buffer (pH 7.0).

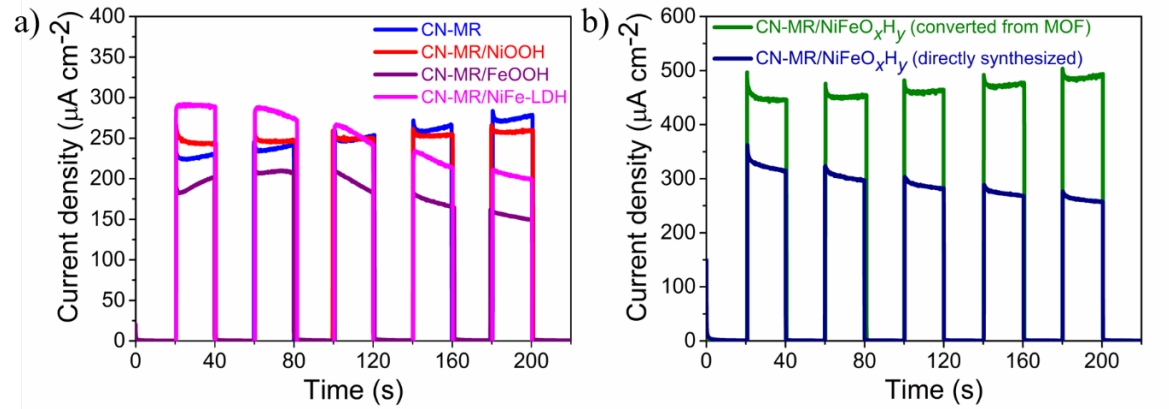

Figure S29. Chronoamperometric characterization of CN-MR electrodes containing Ni- and Fe-based OER cocatalysts. Photocurrent densities measured at 1.23 V *vs.* RHE in 0.1 M KOH. a) Ni- and Fe-based OER cocatalysts deposited on CN-MR film and b) comparison between directly-synthesized $NiFeO_xH_y$ (electrochemical deposition) and $NiFeO_xH_y$ converted from MOF (this work).

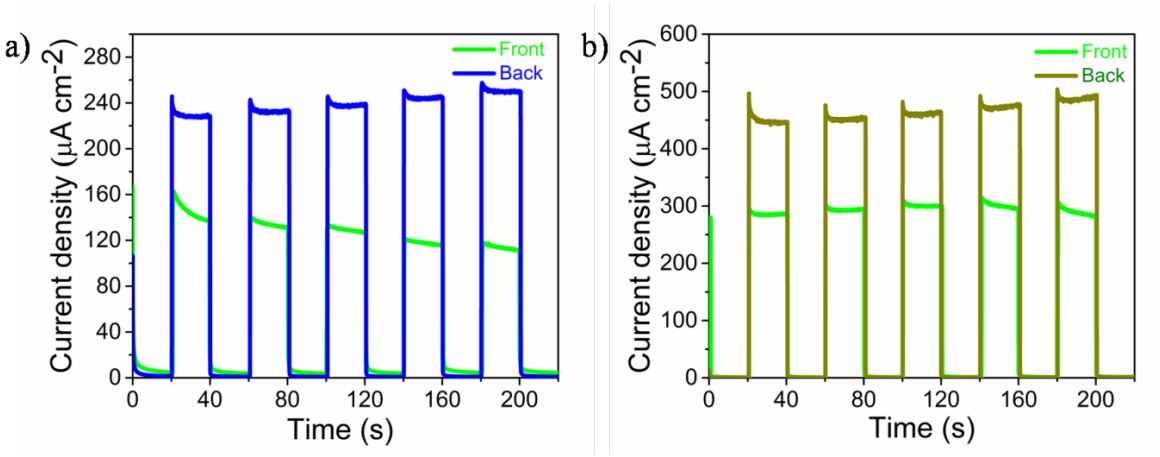

Figure S30. Chronoamperometric characterization under front- /back-side illumination. Photocurrent densities upon illumination from the front- and back-sides. a) CN-MR and b) CN-MR/NiFeO$_x$H$_y$ electrodes at 1.23 V *vs.* RHE in 0.1 M KOH.

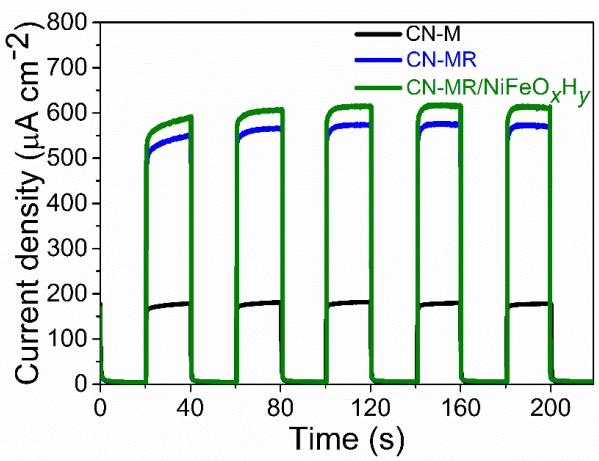

Figure S31. Photocurrent densities (chronoamperometry) of CN electrodes at 1.23 V *vs.* RHE in 0.1 M KOH aqueous solution containing 10% TEOA (v/v) as a hole scavenger.

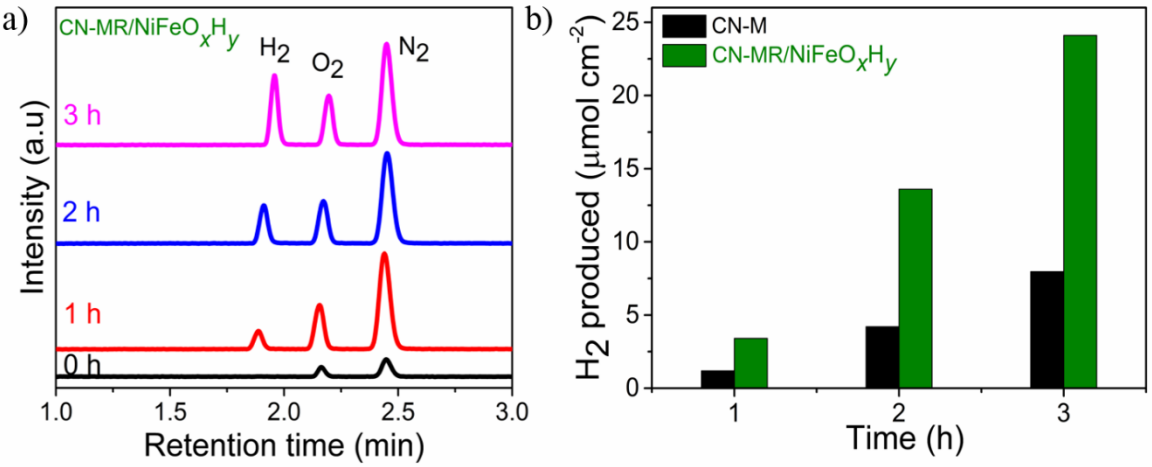

Figure S32. HER quantification. a) Gas chromatographs from a CN-MR/NiFeO$_x$H$_y$ electrode for H_2 production (0, 1, 2, and 3 h). The electrodes are biased at 1.23 V *vs.* RHE, while the electrolyte is 0.1 M KOH containing 10% (v/v) TEOA and b) H_2 production of CN-M (black) and CN-MR/NiFeO$_x$H$_y$ as a function of time.

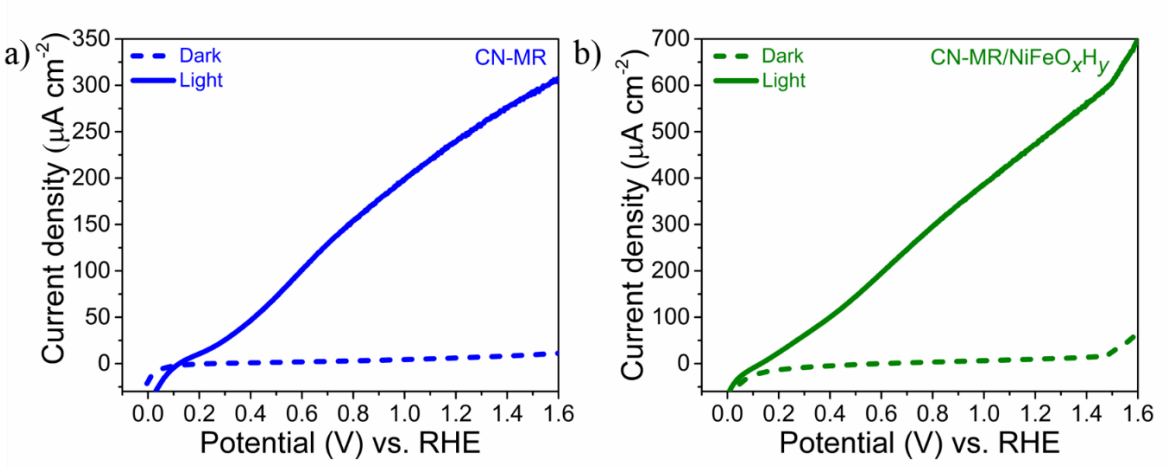

Figure S33. Linear sweep voltammetry (LSV) curves of CN-MR and CN-MR/NiFeO$_x$H$_y$. a) *j–V* characteristics of CN-MR (blue) and b) CN-MR/NiFeO$_x$H$_y$ (green) in 0.1 M KOH in the dark (dashed) and under illumination (complete).

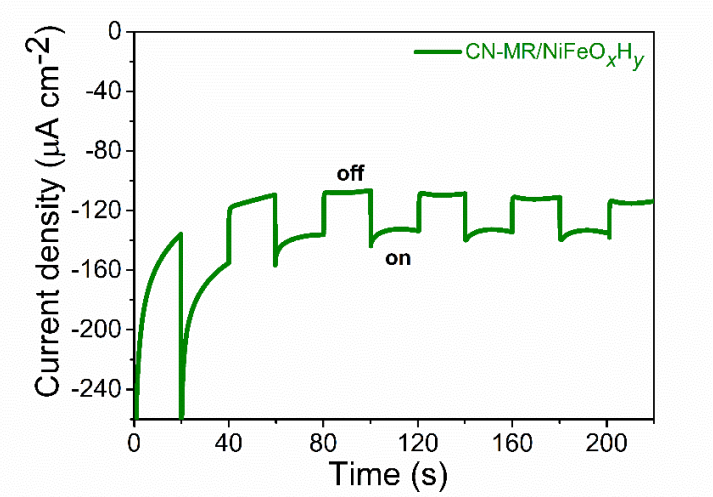

Figure S34. Photocurrent densities (chronoamperometry) of CN-MR/NiFeO$_x$H$_y$ measured at 0 V *vs*. RHE in 0.1 M KOH.

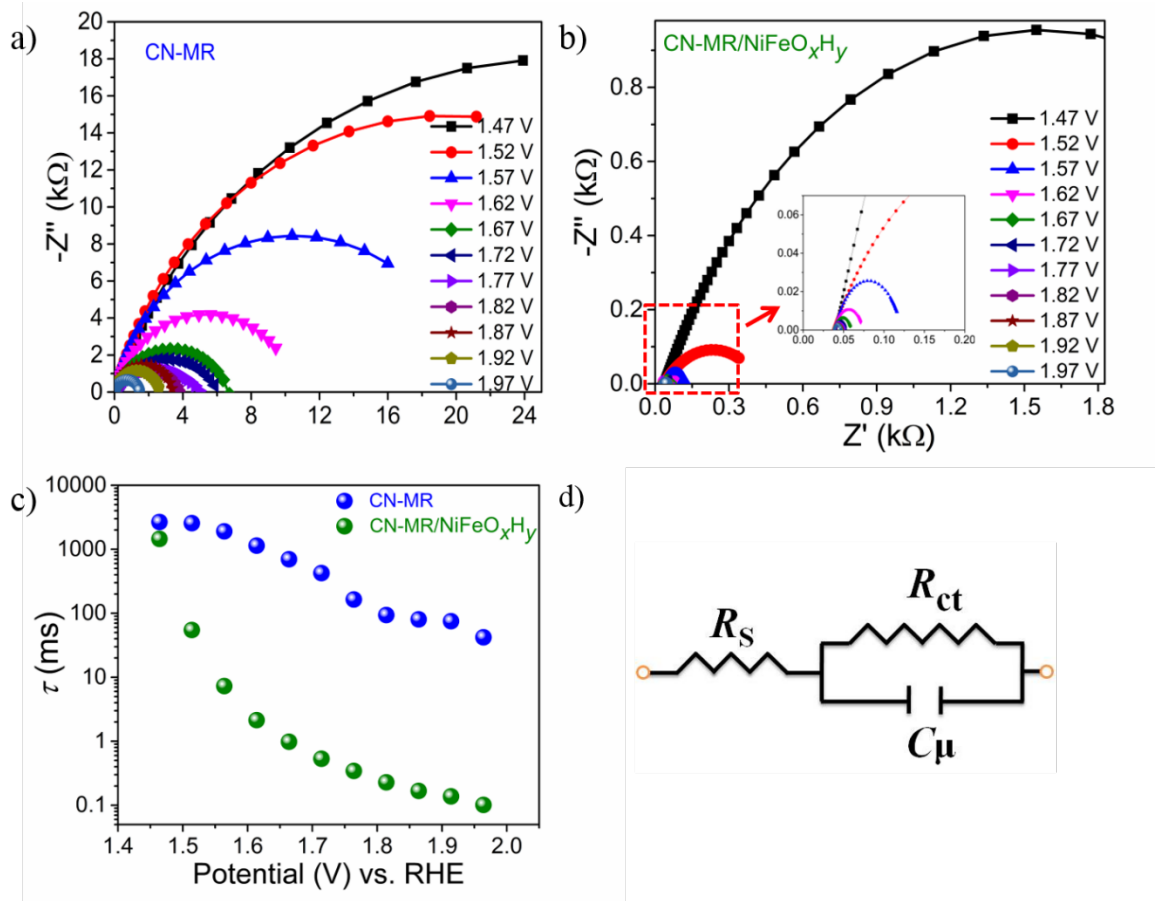

Figure S35. Additional EIS characterization of the photoelectrodes. Nyquist plots of a) CN-MR and b) CN-MR/NiFeO$_x$H$_y$, at different applied voltage biases, fitted using the electrochemical equivalent circuit. c) Calculated time constant (τ) of the two CN electrodes at different potentials (*vs.* RHE) in 0.1 M KOH aqueous solution (the τ values were calculated using equation 3). d) The equivalent circuit that was used for fitting: the R_{ct} and chemical capacitance (C_μ) values were obtained by fitting the semicircles of the Nyquist plots.

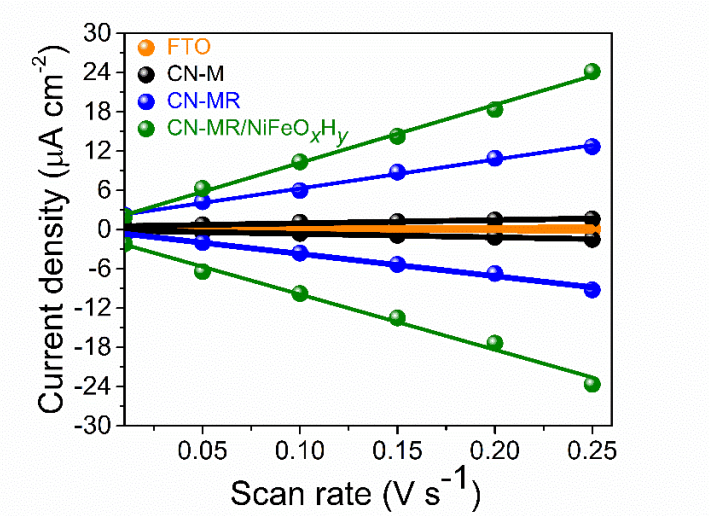

Figure S36. Cathodic and anodic charging currents of CN electrodes at 0.1 V *vs.* Ag/AgCl as a function of scan rate.

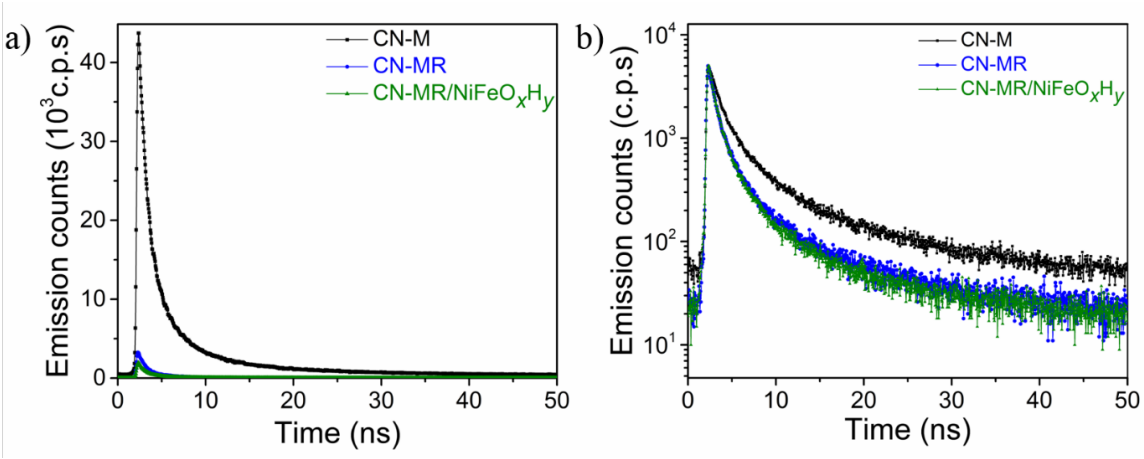

Figure S37. Time-resolved fluorescence decay spectra of CN electrodes. a) emission counts and b) lifetime. Excitation wavelength: 405 nm and emission wavelength: 475 nm.

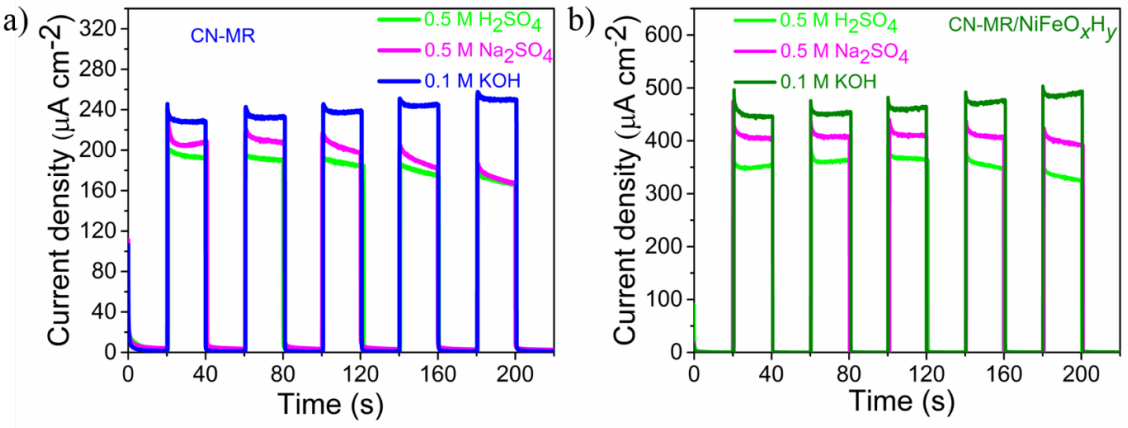

Figure S38. Chronoamperometry at different acidity environments. Photocurrent densities of a) CN-MR and b) CN-MR/NiFeO$_x$H$_y$ electrodes in alkaline 0.1 M KOH (pH = 13.1), neutral 0.5 M Na_2SO_4 (pH = 6.27, magenta), and strongly acidic 0.5 M H_2SO_4 (pH = 0.27, light green) aqueous solutions.

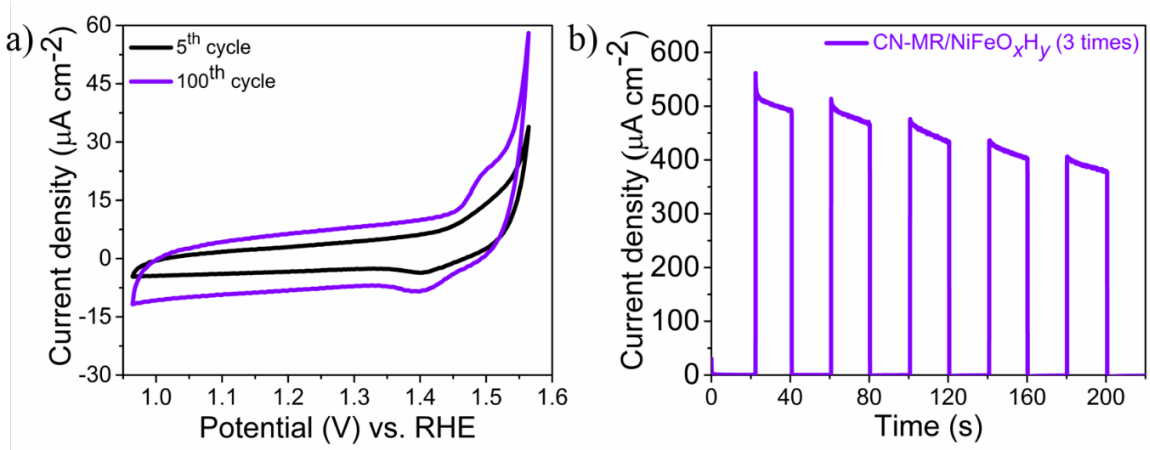

Figure S39. Electrochemical characterization of photoelectrodes with high MOF loading. a) Cyclic voltammograms and b) chronoamperometry in 0.1 M KOH of CN-MR/NiFeO$_x$H$_y$ (3 times), i.e., photoelectrodes with a 3-fold increase in the MOF pre-catalyst content.

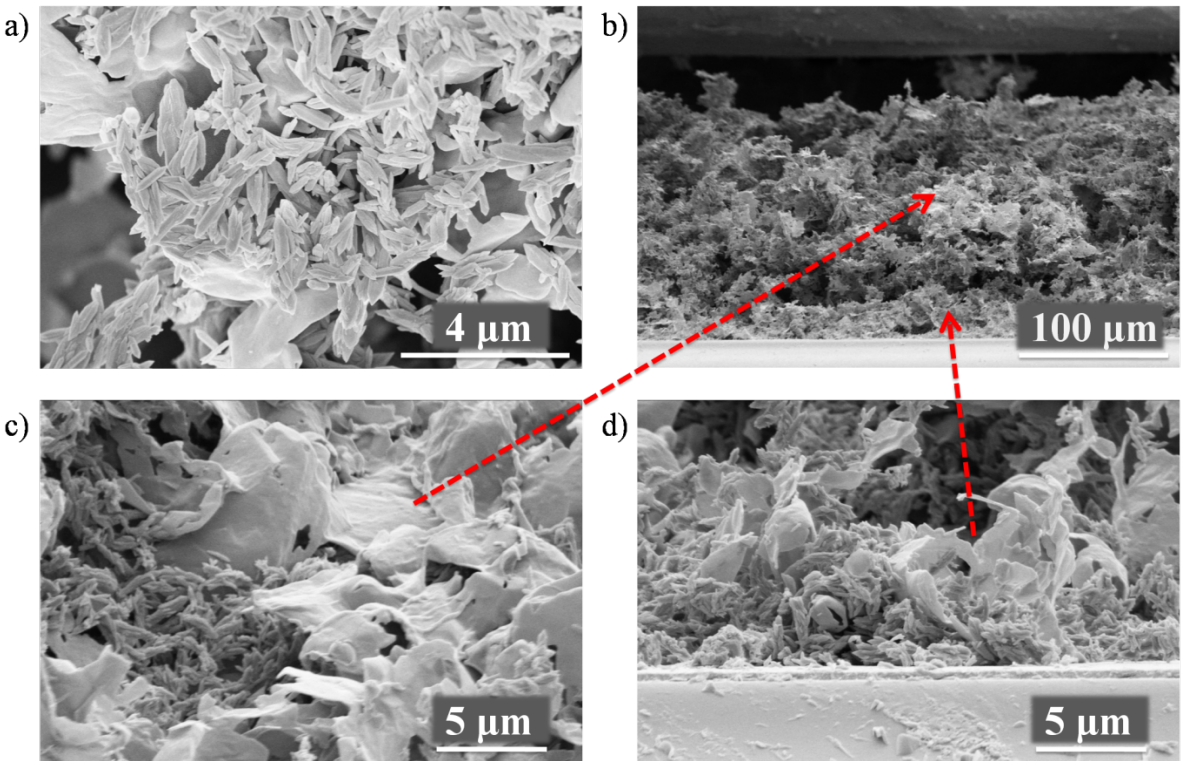

Figure S40. SEM images of high MOF loading electrodes. a) Top-view and b) cross-section CN-MR/MOF (3 times), i.e., CN films after a 3-fold increase of the MOF content. c) and d) additional magnified images the MOF deposition at different positions of cross section (approximate locations indicated using red dashed arrows).

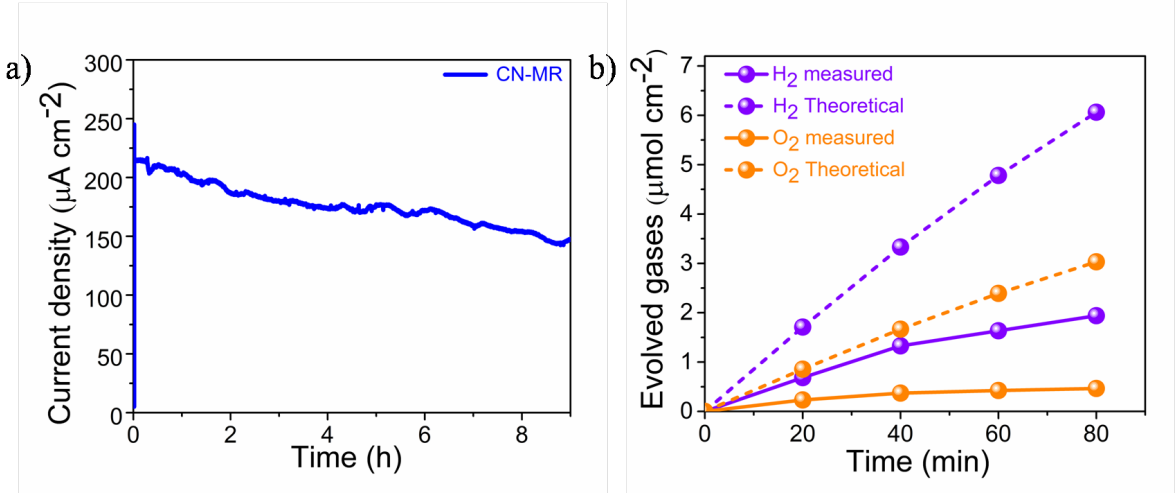

Figure S41. HER and OER over time at alkaline conditions of CN-MR. a) Chronoamperometry (stability test) at 1.23 V *vs.* RHE under 1-sun illumination for 9 h. b) Evolution of H_2 and O_2 gases measured by gas chromatography (dashed lines correspond to the amount of H_2 ($e^-/2$) and O_2 ($e^-/4$) calculated from the photocurrent measurements).

Figure S42. Digital image of the photoelectrochemical water splitting setup. The amount of oxygen and hydrogen evolved from the photoelectrode and the Pt counter electrode were measured in air-tight two-compartment cell with three-electrode configuration by using Ag/AgCl reference electrode.

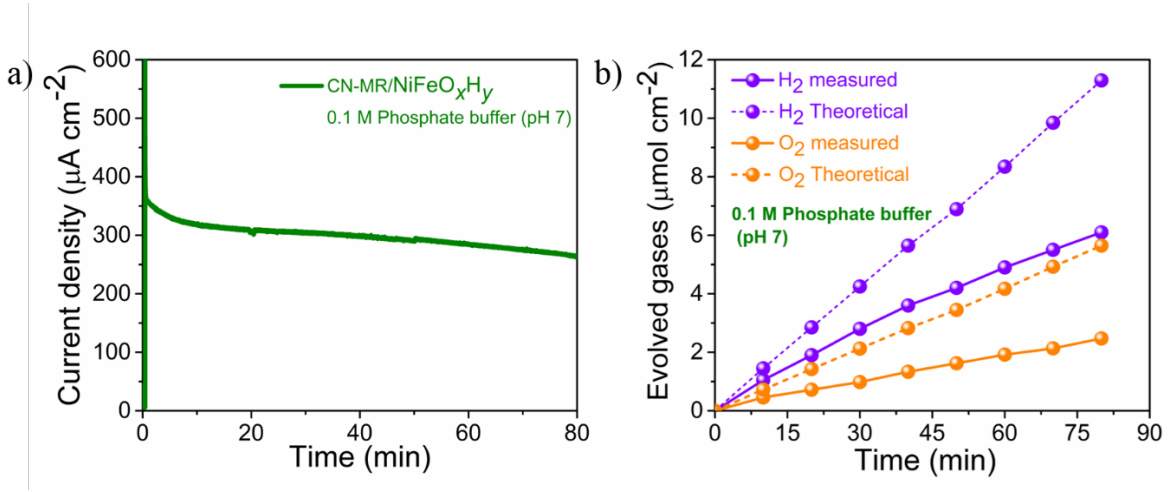

Figure S43. HER and OER over time at neutral conditions of CN-MR/NiFeO$_x$H$_y$. a) Chronoamperometry (stability test) at 1.23 V *vs.* RHE, recorded in a phosphate buffer (0.1 M; pH 7) solution under 1-sun illumination for H_2 and O_2 evolution measurements. b) Evolution of H_2 and O_2 gases measured by gas chromatography. The calculated faradaic efficiency of CN-MR/NiFeO$_x$H$_y$ photoanode for H_2 and O_2 evolution was 54.0% and 43.8%, respectively.

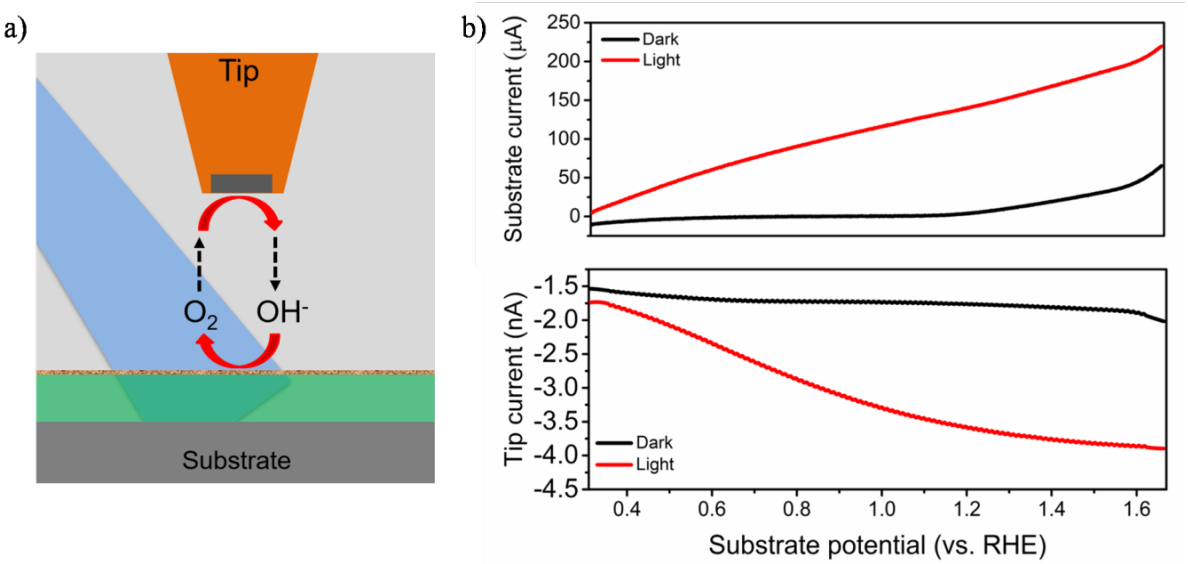

Figure S44. SECM analysis. a) Schematic presentation of the scanning electrochemical microscopy (SECM)-based substrate-generation tip-collection experiment for direct detection of photoelectrochemical O_2 evolution. b) Substrate-generation tip-collection LSV curves of CN-MR/NiFeO$_x$H$_y$ in the dark (black) and under 405 nm (LED source) illumination (red).

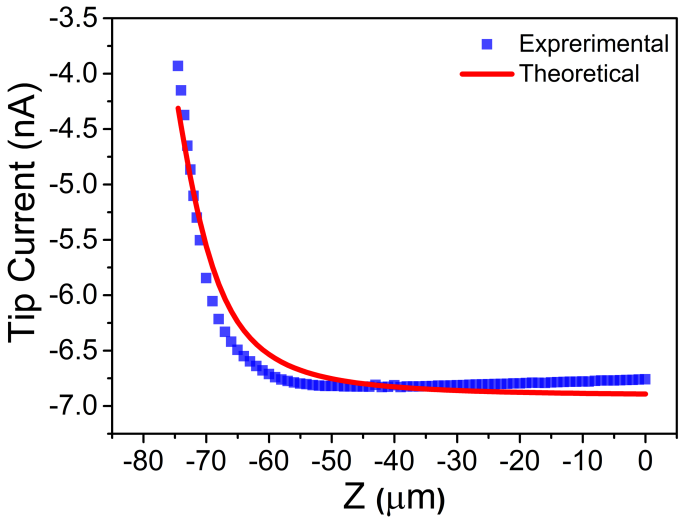

Figure S45. SECM approach curves to the CN-MR/NiFeO$_x$H$_y$ photoanode. The measurement was carried out in an aqueous solution containing 5 mM ferricyanide, 0.1 M KCl, whereas the potential on the tip is held constant at –0.3 V *vs.* Ag/AgCl. The experimental results (blue squares) are compared to the theoretical approach curves obtained from the MIRA simulation software (red line).

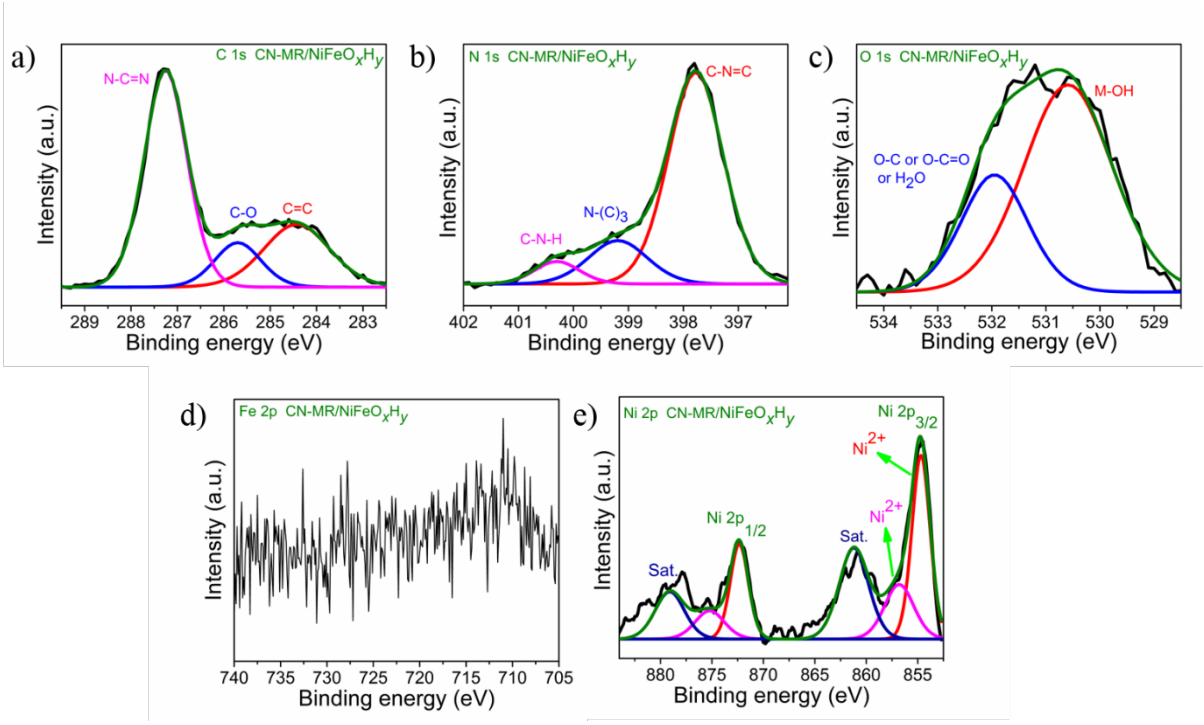

Figure S46. High-resolution XPS spectra of CN-MR/NiFeO$_x$H$_y$ electrodes after a 35 h PEC stability test. a) C 1s, b) N 1s, c) O 1s, d) Fe 2p, and e) Ni 2p. Experimental spectra are plotted in black; green lines represent the fitted spectra; magenta, blue, and red curves are the individual deconvoluted fitted peaks.

Table S3. Elemental analysis of CN-MR/NiFeO$_x$H$_y$ after a stability test obtained by XPS depth profile measurements (measured at ~ 17.5 nm) and SEM-EDS mapping

Element	by XPS (at. %)	by EDS[a] (wt. %)	by EDS[a] (at. %)
C	47.25 (1s)	52.9 ± 0.8	50.7 ± 0.8
N	37.96 (1s)	36.1 ± 0.4	40.4 ± 0.5
O	13.55 (1s)	10.4 ± 0.5	8.7 ± 0.4
Fe	–	0.3 ± 0.1	0.06 ± 0.02
Ni	1.25 (2p)	0.4 ± 0.1	0.09 ± 0.02

[a]all quantification using K-edge lines

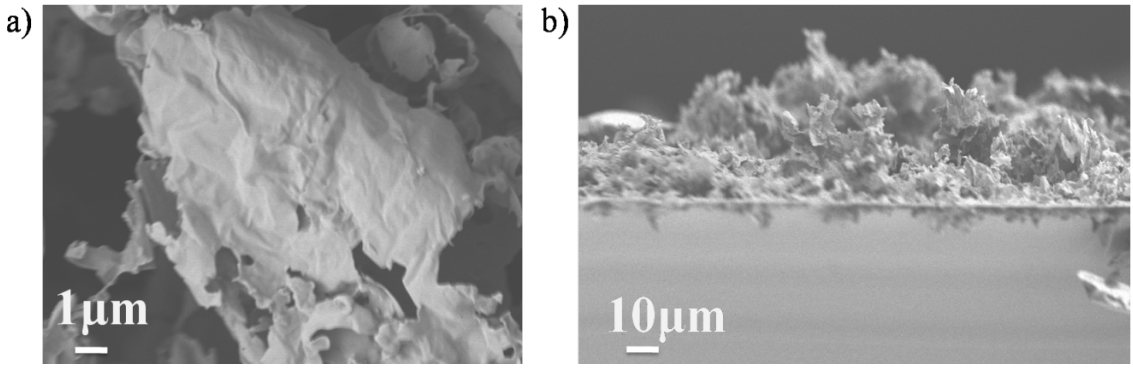

Figure S47. SEM images of CN-MR/NiFeO$_x$H$_y$ after a stability test. a) Top view and b) cross-section.

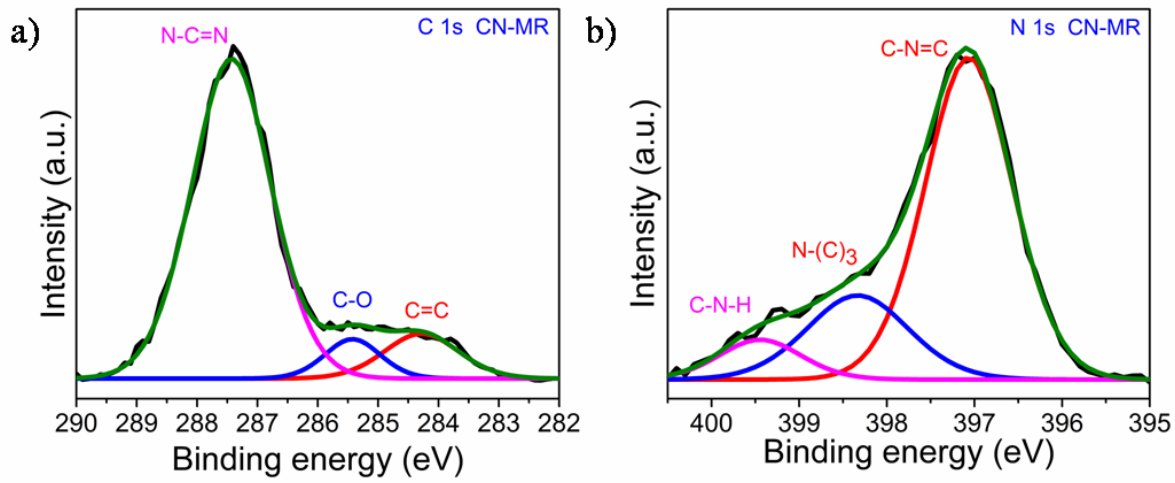

Figure S48. High-resolution XPS spectra after PEC stability test of CN-MR. a) C1s and b) N1s spectra of CN-MR electrodes. Experimental spectra are plotted in black; green lines represent the fitted spectra; magenta, blue, and red curves are the individual deconvoluted fitted peaks.

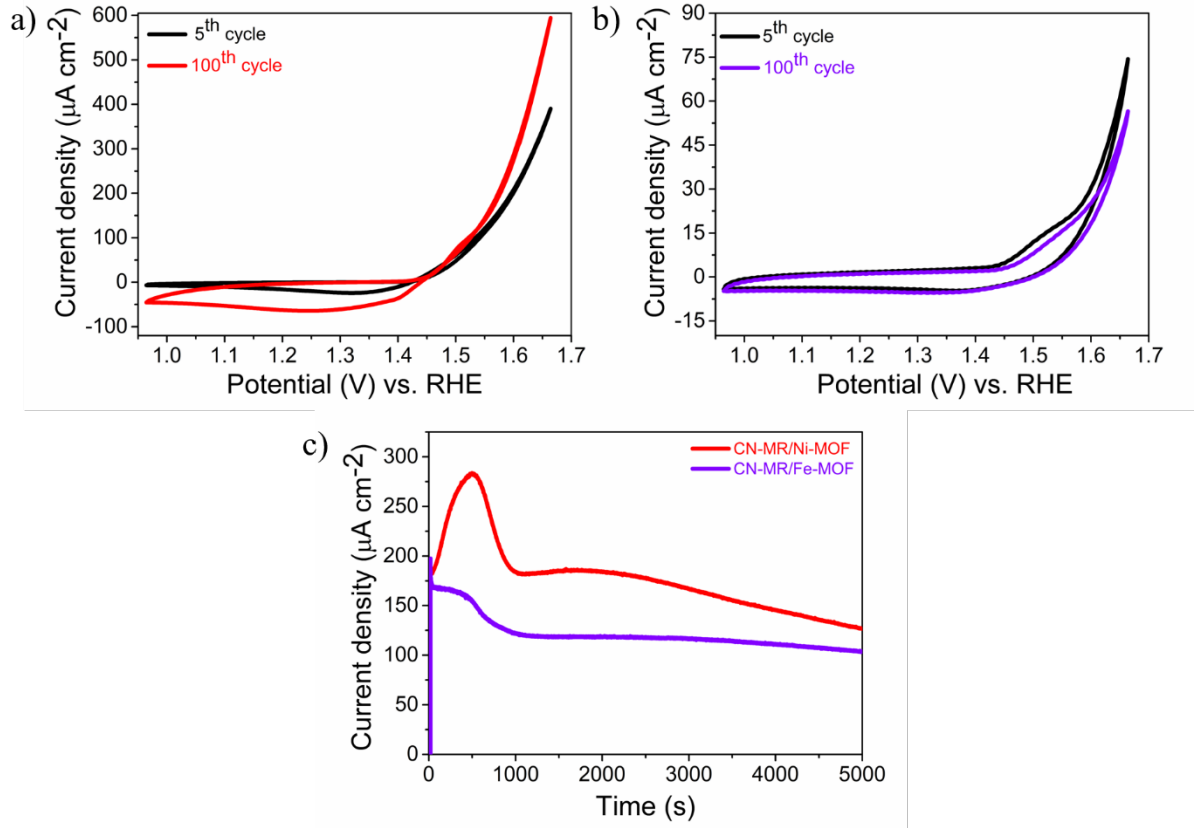

Figure S49. Electrochemical and photoelectrochemical characterization of photoanodes modified with cocatalysts derived from monoatomic MOFs. a) Cyclic voltammograms of CN-MR/Ni-MOF in 0.1 M KOH. b) Cyclic voltammograms of CN-MR/Fe-MOF in 0.1 M KOH. c) Chronoamperometry (stability test) of CN-MR/Ni-MOF and CN-MR/Fe-MOF electrodes (after electrochemical activation) at 1.23 V *vs*. RHE in 0.1 M KOH.

Table S4. PEC performance summary of CN-based photoanodes

CN-based photoanodes (doping materials)	Photocurrent (μA cm^{-2})	Applied potential	Onset potential vs. RHE	Electrolyte	Faradaic efficiency for OER	Light intensity	Reference
CN-MR/$NiFeO_xH_y$	472	1.23 V *vs.* RHE	0.034	0.1 M KOH (pH 13.1)	83%	100 mW cm^{-2}, 1.5 AM	This work
	598	1.23 V *vs.* RHE	N/A	10% (v/v) TEOA in 0.1 M KOH	N/A		
CN-MR (rGO doped)	241	1.23 V *vs.* RHE	0.12	0.1 M KOH (pH 13.1)	15.6%	100 mW cm^{-2}, 1.5 AM	This work
	563	1.23 V *vs.* RHE	N/A	10% (v/v) TEOA in 0.1 M KOH	N/A		
CN-MSG/M (S and rGO doped)	270	1.23 V *vs.* RHE	0.0012	0.1 M KOH (pH 13.1)	28.7%	100 mW cm^{-2}, 1.5 AM	[9]
	510	1.23 V *vs.* RHE	N/A	10% (v/v) TEOA in 0.1 M KOH	N/A		
CN_{TM} (S doped)	353	1.23 V *vs.* RHE	0.32	0.1 M KOH (pH 13)	52%	100 mW cm^{-2}, 1.5 AM	[10]
	565	1.23 V *vs.* RHE	N/A	10% (v/v) TEOA in 0.1 M KOH	N/A		
Compact CN (melem–melamine adducts)	133	1.23 V *vs.* RHE	0.147	0.1 M KOH (pH 13)	N/A	100 mW cm^{-2}, 1.5 AM	[11]
	383	1.23 V *vs.* RHE	N/A	10% (v/v) TEOA in 0.1 M KOH	N/A		
3% Ni-CN	69.8	1.23 V *vs.* RHE	0.71	0.1 M KOH (pH 13)	N/A	100 mW cm^{-2}, 1.5 AM	[12]
In situ grown porous CN/rGO film (rGO doped)	124.5	1.23 V *vs.* RHE	0.35	0.1 M KOH (pH 13)	N/A	100 mW cm^{-2}, 1.5 AM	[13]
	272	1.23 V vs. RHE	N/A	10% (v/v) TEOA in 0.1 M KOH	N/A		
Crystalline CN film	116	1.23 V vs. RHE	0.25	0.1 M KOH (pH 13)	N/A	100 mW cm^{-2}, 1.5 AM	[14]
	245	1.23 *vs.* RHE	N/A	10% (v/v) TEOA in 0.1 M KOH	N/A		
Phosphorylated CN (P doped)	120	1.23 V *vs.* RHE	~ 0.11	1.0 M NaOH	N/A	100 mW cm^{-2}, 1.5 AM	[15]
2,6-Diaminopyridine modified g-CN (CMD5)	100	1.23 V *vs.* RHE	N/A	0.1 M Na_2SO_4 + 0.1 M Na_2SO_3 + 0.01M Na_2S (pH 11.6)	N/A	100 mW cm^{-2}, 1.5 AM	[16]
B-doped CN	103.2	1.23 V *vs.* RHE	~0.4	0.1 M Na_2SO_4 (pH 6.5)	N/A	100 mW cm^{-2}, AM 1.5	[17]
S-doped CN	60	1.23 V *vs.* RHE	N/A	0.1 M KOH	N/A	50 W (LED) white light	[18]
CN–rGO film	72	1.23 V *vs.* RHE	0.75	0.1 M KOH (pH 13)	N/A	100 mW cm^{-2}, AM 1.5	[1]
	660	1.23 V *vs.* RHE	N/A	10% (v/v) TEOA in 0.1 M KOH	N/A		
g-CN film (C doped)	228.2	1.23 V *vs.* RHE	N/A	0.2 M Na_2SO_4 (pH 6.0)	N/A	100 mW cm^{-2}, 1.5 AM	[19]
CN and P- and B-doped CN heterojunction	150	1.23 V *vs.* RHE	N/A	0.1 M Na_2SO_4 (pH 6.5)	N/A	100 mW cm^{-2}, 1.5 AM	[20]
g-CN	63	1.23 V *vs.* RHE	N/A	0.1 M Na_2SO_4 (pH 7)	N/A	100 mW cm^{-2}, 1.5 AM	[21]

g-CN/Co-Pi	40	0.5 V *vs.* Ag/AgCl	N/A	0.01 M Na_2SO_4	N/A	300 W Xe arc lamp (λ > 420 nm)	[22]
g-CN/NiCo-LDH	11.8	0.6 V *vs.* SCE	N/A	0.2 M Na_2SO_4	N/A	200 W Xe lamp (λ > 420 nm)	[23]

Supplementary Information References

[1] G. Peng, M. Volokh, J. Tzadikov, J. Sun, M. Shalom, *Adv. Energy Mater.* **2018**, *8*, 1800566.
[2] F. Fina, S. K. Callear, G. M. Carins, J. T. S. Irvine, *Chem. Mater.* **2015**, *27*, 2612.
[3] a) B. V. Lotsch, M. Döblinger, J. Sehnert, L. Seyfarth, J. Senker, O. Oeckler, W. Schnick, *Chem. Eur. J.* **2007**, *13*, 4969-4980; b) N. Karjule, J. Barrio, J. Tzadikov, M. Shalom, *Chem. Eur. J.* **2020**, *26*, 6622.
[4] C. Singh, I. Liberman, R. Shimoni, R. Ifraemov, I. Hod, *J. Phys. Chem. Lett.* **2019**, *10*, 3630.
[5] F. Sun, G. Wang, Y. Ding, C. Wang, B. Yuan, Y. Lin, *Adv. Energy Mater.* **2018**, *8*, 1800584.
[6] W. He, H.-M. Gao, R. Shimoni, Z.-Y. Lu, I. Hod, *ACS Appl. Energy Mater.* **2019**, *2*, 2138.
[7] L. Bai, S. Lee, X. Hu, *Angew. Chem. Int. Ed.* **2020**, *59*, 2.
[8] F. Wu, X. Guo, G. Hao, Y. Hu, W. Jiang, *Nanoscale* **2019**, *11*, 14785.
[9] N. Karjule, J. Barrio, L. Xing, M. Volokh, M. Shalom, *Nano Lett.* **2020**, *20*, 4618.
[10] J. Qin, J. Barrio, G. Peng, J. Tzadikov, L. Abisdris, M. Volokh, M. Shalom, *Nat. Commun.* **2020**, *11*, 4701.
[11] J. Xia, N. Karjule, L. Abisdris, M. Volokh, M. Shalom, *Chem. Mater.* **2020**, *32*, 5845.
[12] W. Zhang, J. Albero, L. Xi, K. M. Lange, H. Garcia, X. Wang, M. Shalom, *ACS Appl. Mater. Interfaces* **2017**, *9*, 32667.
[13] G. Peng, J. Qin, M. Volokh, C. Liu, M. Shalom, *J. Mater. Chem. A* **2019**, *7*, 11718.
[14] G. Peng, J. Albero, H. Garcia, M. Shalom, *Angew. Chem. Int. Ed.* **2018**, *57*, 15807.
[15] Y. Fang, X. Li, X. Wang, *ChemSusChem* **2019**, *12*, 2605.
[16] J. Bian, L. Xi, C. Huang, K. M. Lange, R.-Q. Zhang, M. Shalom, *Adv. Energy Mater.* **2016**, *6*, 1600263.
[17] Q. Ruan, W. Luo, J. Xie, Y. Wang, X. Liu, Z. Bai, C. J. Carmalt, J. Tang, *Angew. Chem. Int. Ed.* **2017**, *56*, 8221.
[18] J. Xu, S. Cao, T. Brenner, X. Yang, J. Yu, M. Antonietti, M. Shalom, *Adv. Funct. Mater.* **2015**, *25*, 6265.
[19] W. Xiong, S. Chen, M. Huang, Z. Wang, Z. Lu, R.-Q. Zhang, *ChemSusChem* **2018**, *11*, 2497.
[20] P. Luan, Q. Meng, J. Wu, Q. Li, X. Zhang, Y. Zhang, L. A. O'Dell, S. R. Raga, J. Pringle, J. C. Griffith, C. Sun, U. Bach, J. Zhang, *ChemSusChem* **2020**, *13*, 328.
[21] X. Lv, M. Cao, W. Shi, M. Wang, Y. Shen, *Carbon* **2017**, *117*, 343.
[22] L. Ge, C. Han, X. Xiao, L. Guo, *Appl. Catal. B Environ.* **2013**, *142-143*, 414.
[23] X. Fan, T. Wang, B. Gao, X. Xie, S. Zhang, X. Meng, H. Gong, Y. Guo, X. Huang, J. He, *Catal. Today* **2019**, *335*, 423.